Command Shaping for Vibration Reduction in Nonlinear Cabled Systems

A Thesis
Presented to
The Academic Faculty

by

David F. Blackburn

In Partial Fulfillment
of the Requirements for the Degree
Master of Science

George W. Woodruff School of Mechanical Engineering
Georgia Institute of Technology
August 2006

Command Shaping for Vibration Reduction in Nonlinear Cabled Systems

Approved by:

William Singhose, Ph.D., Advisor
School of Mechanical Engineering
Georgia Institute of Technology

Nader Sadegh, Ph.D.
School of Mechanical Engineering
Georgia Institute of Technology

John-Paul Clarke, Sc.D.
School of Aerospace Engineering
Georgia Institute of Technology

Date Approved: July 4, 2006

ACKNOWLEDGEMENTS

I would like to thank all of the people who made this thesis possible. First, I would like to thank my advisor, William Singhose, for all of his help and guidance throughout my time here at Georgia Tech. I would like to thank James Kitchen, Vlad Patrangenaru, and Jason Lawrence at Georgia Tech for their help on the advanced tower crane shaper, as well as Tatsuaki Kamoi and Ayako Taura at Tokyo Tech. I would like to thank Michael Robertson and Takeo Watanabe for their work on constant orbit flexible tether dynamics. I would also like to thank Arun Banerjee for supplying the dynamic model for orbit boosting of electrodynamic tethers.

Funding for my orbit boosting research was provided through a Graduate Student Research Program grant from NASA Marshall Space Flight Center. Siemens Energy and Automation, the Georgia Tech PURA, and the 21^{st} Century Center of Excellence in Robotics at the Tokyo Institute of Technology provided equipment and funding for the experimental tower crane. Lastly, I would like to thank my lab group at Georgia Tech for their constant support and encouragement.

TABLE OF CONTENTS

LIST OF TABLES

LIST OF FIGURES

SUMMARY

Cables are an integral part of many engineering systems; thus, the control of cables and systems containing cables is an important problem to address. This thesis proposes to use command shaping techniques to reduce command-induced vibration in two cabled systems, a tower crane and an electrodynamic tethered satellite system in low Earth orbit. Systems containing cables often exhibit important nonlinear dynamics, which complicates the application of command shaping.

As a first step to demonstrate the effectiveness of command shaping techniques for nonlinear cabled systems, nonlinear tower crane dynamics are investigated. A novel command generation technique for the slewing of tower cranes is presented, and experimental results demonstrate its increased effectiveness. Once improvement of tower crane dynamics has been demonstrated, space tether dynamics are considered.

Electrodynamic tethers have the promise to become invaluable propulsive actuators for orbit boost and station keeping. Using electrodynamic tethers, it is possible to boost orbits without the use of propellant because electrical energy is used to produce a Lorentz force that creates orbit boost. Furthermore, electrodynamic tether deboost makes it possible to accelerate the deorbiting of spent rocket stages and other space debris to reduce clutter in the space environment. Unfortunately, the Lorentz force pushes transversely on the cable tether, thereby producing a significant amount of vibration and libration.

This thesis proposes to use command shaping techniques to reduce the command-induced vibration from a boosting operation. Intelligent command generation will significantly reduce the amount of tether libration and string vibration. First, flexible tether dynamics in a constant, circular orbit are investigated. The work is then expanded to include the effects of orbit boosting. The robustness of the command generation techniques is established through numerical simulation.

CHAPTER I

INTRODUCTION

Cables are an important part of many engineering systems. Cable-driven robots have received a lot of attention lately as a promising way to achieve high-speed motion in large working areas with relatively little hardware [5, 6, 11, 13]. For example, cable-suspended cameras have been successfully implemented in many sports arenas to get a "first-person" perspective of the action.

In addition to parallel platform type devices, axially moving string models can be applied to high speed elevators, cranes, space tethers, and other systems. Cables allow cranes to easily hoist and move large payloads, but their flexibility leads to complicated oscillation problems. Numerous applications exist for cable tethers in space. The space environment further complicates their dynamics with gravity gradient effects and the absence of significant damping. This lack of damping combines with long periods of oscillation to present a very challenging control problem.

Much work has been done in the area of controlling strings, which are essentially very lightweight cables. Zhang and Chen derived a feedback control law for controlling transverse vibrations in axially moving strings actuated via a tensioner. This is readily applicable to vibration reduction in a serpentine-belt drive system [46]. Yang, *et al.* developed a robust boundary controller using hydraulic actuation at one boundary to accomplish the same objective [45]. Alli and Singh used Lyapunov and frequency domain approaches to design controllers for rest-to-rest motions of a bar governed by the wave equation. They used root-locus techniques to determine optimal controller gains for collocated and non-collocated sensor-actuator pairs [1].

This thesis develops intelligent command generation techniques for the control of two systems containing important cable dynamics. First, a novel command shaping approach for tower crane slewing motion is presented. Experimental results on a portable tower crane

[15] at the Tokyo Institute of Technology are used to verify the effectiveness of the proposed approach. Then, novel input shaping techniques are applied to nonlinear space tether dynamics. The effectiveness of these techniques is tested on dynamic models obtained from the pre-existing literature and from a joint collaboration with Lockheed Martin Advanced Technology Center.

1.1 Input Shaping

Input shaping is a method of command filtering that allows many oscillatory systems to be moved without inducing residual vibration. Input shaping is implemented by convolving a series of impulses, known as the input shaper, with a desired reference command. This produces a command that will drive the system while limiting residual vibration [33, 23]. This process is illustrated in Figure 1 with a step reference input. Input shaping is attractive because detailed system knowledge is not necessary: only estimates of the natural frequencies and damping ratios of the dominant modes of vibration are required to design the input shaper.

Input shaping relies on the superposition of impulse responses of a second-order system to reduce residual vibration. To design the input shaper, a measure of the residual vibration as a function of the shaper is needed. The response of a second-order harmonic oscillator of frequency ω and damping ratio ζ to a series of n impulses is divided by its response to a single impulse to obtain this measure. This percentage vibration is given by [23]

$$V = e^{-\zeta\omega t_n}\sqrt{\left[C\left(\omega,\zeta\right)\right]^2 + \left[S\left(\omega,\zeta\right)\right]^2} \tag{1}$$

where

$$C\left(\omega,\zeta\right) = \sum_{i=1}^{n} A_i e^{\zeta\omega t_i}\cos\left(\omega\sqrt{1-\zeta^2}t_i\right) \tag{2a}$$

$$S\left(\omega,\zeta\right) = \sum_{i=1}^{n} A_i e^{\zeta\omega t_i}\sin\left(\omega\sqrt{1-\zeta^2}t_i\right) \tag{2b}$$

and A_i and t_i are the amplitudes and time locations of the impulses.

The earliest form of input shaping was developed by O. J. M. Smith in the late 1950's [33]. His posicast control method suggested replacing a single step input with two step

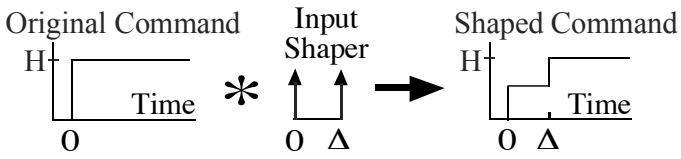

Figure 1: Input shaping process

inputs of smaller magnitude, one of which is delayed by one-half period of vibration. This will cause destructive interference in the responses to each step input and theoretically cancel all vibration induced by each input. This is equivalent to convolving the original step with two impulses. These impulses are designed by satisfying (1) with V set to zero, ensuring zero residual vibration with a perfect model. For this reason, the shaper designed with these constraint equations is generally referred to as the Zero-Vibration (ZV) shaper [33, 23]. On closer investigation, to make (1) equal zero, both (2a) and (2b) must equal zero independently. This yields two constraint equations. In order to fully specify the times and amplitudes of the two impulses of the ZV shaper, more constraints are needed. To make sure that the shaped commands will be bounded and have the same setpoint as the unshaped commands, the impulse magnitudes are generally required to be positive and to sum to one. That is,

$$A_i > 0\,, \quad \sum_{i=1}^{n} A_i = 1 \tag{3}$$

In order to maximize the performance of the input shaper, the first impulse is set to occur at time $t_1 = 0$ and the time of the last impulse, t_n is minimized. This is enough to fully constrain the ZV shaper, and the impulse times and amplitudes are given by [33, 23]

$$\begin{bmatrix} A_i \\ t_i \end{bmatrix} = \begin{bmatrix} \dfrac{1}{1+K} & \dfrac{K}{1+K} \\ 0 & 0.5T_d \end{bmatrix}, \qquad i = 1, 2 \tag{4}$$

where

$$K = e^{\left(\dfrac{-\zeta\pi}{\sqrt{1-\zeta^2}}\right)} \tag{5}$$

and T_d is the damped period of vibration.

While the ZV shaper will theoretically yield zero-vibration at the modeling frequency, it is very sensitive to modeling errors [38]. This sensitivity to modeling errors prohibited the

ZV shaper from practical use on many systems. Singer and Seering were the first to develop an input shaping technique robust enough to be used in practical applications. To reduce the sensitivity of the input shaper to errors in natural frequency, they set the derivative of the vibration with respect to the natural frequency to zero at the modeling frequency. This adds the constraint equation [23]

$$0 = \frac{\partial}{\partial \omega}\left[e^{-\zeta \omega t_n}\sqrt{\left[C\left(\omega,\zeta\right)\right]^2 + \left[S\left(\omega,\zeta\right)\right]^2}\right]_{\omega=\omega_m} \tag{6}$$

Enforcing this constraint on residual vibration requires the addition of another impulse. This yields the following impulse times and amplitudes [23]:

$$\begin{bmatrix} A_i \\ t_i \end{bmatrix} = \begin{bmatrix} \frac{1}{(1+K)^2} & \frac{2K}{(1+K)^2} & \frac{K^2}{(1+K)^2} \\ 0 & 0.5T_d & T_d \end{bmatrix}, \qquad i = 1,2,3 \tag{7}$$

where K is the same as before. The time penalty incurred for the added robustness of this shaper is one extra half-period of vibration, as can be seen from the impulse time locations in (7). Because this shaper adds the robustness constraint of zero-derivative at the modeling frequency, it is called the Zero-Vibration and Derivative (ZVD) shaper. This process of setting derivatives equal to zero can be continued with higher order derivatives. Each higher order derivative constraint requires the addition of another impulse. This increases the robustness of the shaper while continuing to lengthen the shaper, thereby increasing the rise time of the system.

The robustness of various input shapers can be examined graphically through the use of sensitivity curves. These plots graph the percentage residual vibration against the normalized frequency of vibration, ω_a/ω_m, where ω_a is the actual system natural frequency and ω_m is the modeling frequency. Figure 2 shows the sensitivity curves for several common shapers. The solid line corresponds to the ZV shaper given in (4), the dashed line corresponds to the ZVD shaper given in (7), and the others correspond to shapers which will soon be described.

In order to increase the robustness of input shapers without adding impulses, the vibration constraint at ω_m can be relaxed. If, instead of forcing the vibration all the way down to zero, it is allowed to equal some small nonzero value, V_{tol}, then the shaper will

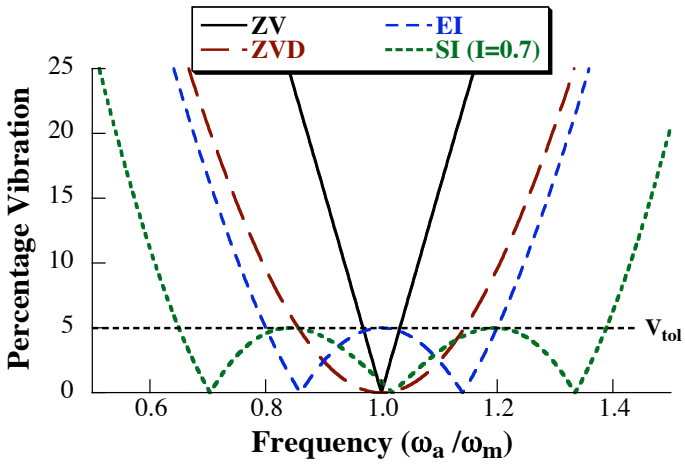

Figure 2: Sensitivity curves for common shapers

be more robust. This shaper design is known as the Extra-Insensitive (EI) shaper [27, 31]. This shaper is constrained by setting the vibration (defined by Equation (1)) equal to V_{tol} and the derivative of the vibration with respect to frequency equal to zero at the modeling frequency. The vibration is then forced to zero at one frequency on either side of the modeling frequency. This produces the hump seen in Figure 2. This shaper increases the robustness to modeling errors by relaxing the unreasonable constraint of zero vibration at the unattainable condition of perfect modeling.

This idea can be extended to the area of Specified-Insensitivity (SI) shapers [24, 32]. The insensitivity of a shaper is defined as the width of the sensitivity curve which lies below a certain vibration threshold. Thus, the 5% insensitivity is the width of the curve which lies completely below 5% residual vibration. If a certain insensitivity is desired, then the shaper constraint equations can be formulated to attain it. An example of this shaper is also illustrated in Figure 2 with a 5% insensitivity of 0.7, that is, the normalized vibration is suppressed for a frequency ratio of 0.65 to 1.35 ($1.35 - 0.65 = 0.7$).

1.1.1 Negative Amplitude Input Shapers

All of the previous shapers have been designed by requiring all of the impulse amplitudes to be positive. Other magnitude constraints can be set to bound the impulse amplitudes. If the impulse amplitudes are assumed to be ± 1, then the result is a family of shapers known as Unity-Magnitude input shapers. The Unity-Magnitude Zero-Vibration (UMZV) shaper

for undamped systems is given by [28]

$$\begin{bmatrix} A_i \\ t_i \end{bmatrix} = \begin{bmatrix} 1 & -1 & 1 \\ 0 & T/6 & T/3 \end{bmatrix}, \qquad i = 1, 2, 3 \tag{8}$$

This reduces the shaper duration from $T/2$ (for a positive ZV shaper) to $T/3$. This decrease in rise time, however, comes with the penalty of high-mode excitation and increased actuator effort. A UMZV shaper may amplify vibration in frequencies higher than the modeling frequency, as can be seen in Figure 3. This high-mode excitation can be alleviated by reducing the magnitude of the negative impulse. By lowering the magnitude, the high-mode excitation is reduced, at the penalty of a slight increase in the system rise time [29].

1.1.2 Input Shaping for Multiple Modes of Vibration

There are also ways to use input shaping to reduce vibration in multiple modes. One way is to design shapers for each individual mode and then convolve them together [12, 26]. The resulting shaper will provide the same vibration reduction at the desired frequencies, with added robustness for higher mode excitation. Another way to design the shaper is to solve the constraint equations for the two modes simultaneously. This method results in vibration reduction near the modeling frequencies, but does not yield as much suppression of the high modes. However, a simultaneous shaper is never longer than a convolved shaper, and it is

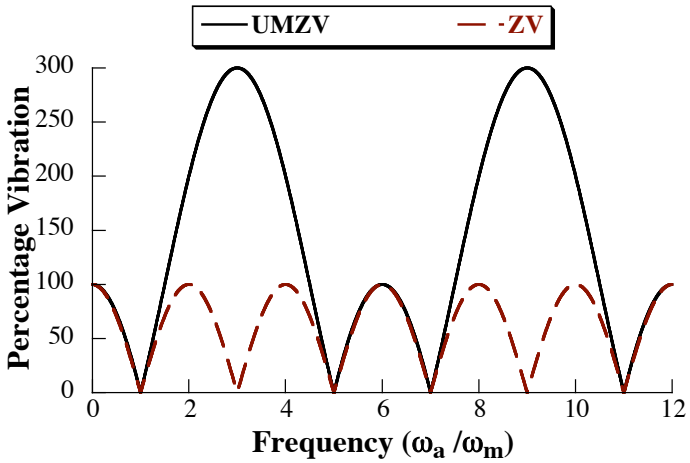

Figure 3: High-mode excitation of UMZV shapers

often significantly shorter. This advantage in speed can be important for slow oscillations [26].

1.1.3 Applications of Input Shaping

Input shaping can be very helpful for reducing vibration in a number of mechanical systems. Two systems of special note included here are cranes and flexible spacecraft. Both cranes and flexible spacecraft often oscillate with long periods and have little to no damping. This means that any vibration induced in the system will continue for a long time unless actively controlled. Thus, input shaping can be extremely useful in reducing command-induced vibrations and increasing the speed and accuracy of these systems.

Singer, Singhose, and Kriikku implemented input shaping on a gantry crane at the Savannah River Technology Center [22]. Fixed Duration (FD) shapers were implemented on this crane, in which the shaper time was held fixed while the robustness to modeling errors was maximized. This process creates a set of shapers for different payload lengths with identical response times. Constant response times are desirable from an operator standpoint, as they do not have to adjust for variable deceleration times. Smith *et al.* applied robust input shaping to trajectory tracking of payloads suspended from multiple robot manipulators [34]. Hong and Hong showed simulation results for point-to-point motions of container cranes using a deflection-limiting input shaping technique and nonlinear vibration stabilization control. This two-stage control scheme successfully limited transient sway angles and residual payload vibration, increasing the speed of container motions [9].

Input shaping has also been studied extensively for applications to flexible spacecraft. Singhose, Bohlke, and Seering developed fuel-efficient pulse profiles for the slewing of flexible spacecraft with on-off reaction jets. These command profiles use all positive pulses in the acceleration phase of rest-to-rest moves and all negative pulses in the deceleration phase. This results in considerable fuel savings with only minimal time penalties versus the time-optimal solutions [30]. Singhose, Banerjee, and Seering applied ZVD constraints to the fuel-efficient slewing of flexible spacecraft while also limiting transient deflection. The method was used to drive the slewing of the waves in space plasma (WISP) antennae simulation with

excellent transient and residual vibration response [25]. Singhose, Derezinski, and Singer introduced one- and two-hump EI shapers for movement of flexible spacecraft with on-off reaction jets. They developed EI shapers for rest-to-rest slews and compared them with ZV and ZVD equivalent shapers. These shapers demonstrated excellent vibration reduction when driving the Draper Laboratory's simulation of the Space Shuttle and its telerobotic manipulator [31].

Hu and Ma applied a technique similar to input shaping called component synthesis vibration suppression (CSVS) combined with Positive Position Feedback (PPF) piezoelectric sensing and actuation to suppress vibration of a slewing spacecraft with on-off thrusters [10]. Banerjee, Pedreiro, and Singhose applied ZVD shaping to the problem of momentum dumping of spacecraft reaction wheels. They also proposed using thrusters to aid in slewing maneuvers while simultaneously dumping momentum. This reduces the time required to slew, eliminates the time required for separate momentum dumping, and uses the same amount of thruster fuel as separate maneuvers. Input shaping is shown to reduce vibration from this maneuver on a model of the next generation space telescope [3].

Watanabe *et al.* applied input shaping to electrodynamic tether operations. Two cases of satellite deorbit and one case of International Space Station reboost were considered in their investigation. Input shaping was shown to drastically reduce tether libration and string vibration during the maneuvers. Robustness of the control system to variations in system parameters was also demonstrated [41].

1.2 Tethers in Space

Although cranes represent a ubiquitous cable-based mechanism on Earth, very few space structures use cable-driven technology. However, the advancement of space tether technology has the potential to change the face of space exploration. It offers the promise of propellantless propulsion using electrodynamic forces. If a current is passed through a long conducting wire traveling through the Earth's magnetic field, a Lorentz force is generated perpendicular to both the current and the magnetic field lines. If this force can be harnessed to boost a spacecraft's orbit, it could extend the useful life of the craft significantly,

greatly reducing the need for refueling missions. However, the proposed tethers can be extremely difficult to control during all phases of their operation, deployment, retrieval, and electrodynamic propulsion. Due to their extreme length and high flexibility, these tethers exhibit very complicated dynamics. Currently, the libration and vibration of space tethers is a major roadblock to mission feasibility.

One of the major applications being considered for electrodynamic tethers is reboost of the International Space Station (ISS). Vas, Thomas, and Scarl performed a study of the application of tether reboost to the ISS. They predicted savings of nearly a billion dollars of propellant over 10 years of operation. They also predict the tether to have little effect on the operation of the space station [40]. Estes, *et al.* also included a study in their paper in 2000 on bare tether electron collection [7].

Another application of tether reboost is the momentum exchange–electrodynamic reboost (MXER) tether system. This system proposes a spinning tether in a highly elliptical low earth orbit (LEO) [36]. This tether would rendezvous with and attach to a smaller satellite and release it after a half-rotation, exchanging momentum and increasing the velocity of the smaller satellite. This will boost the target satellite into a higher orbit and eliminate the need for a second booster rocket, decreasing the cost of launching satellites into high earth orbits. This process is illustrated in Figure 4. The target satellite is approaching for rendezvous in Figure 4(a) and the tether grasps the target in 4(b). It holds the satellite for one half-rotation and releases it in 4(d), transferring momentum to the target satellite. For

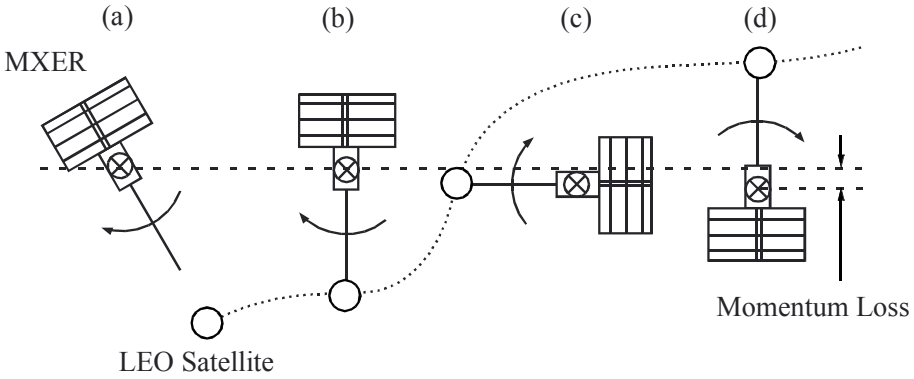

Figure 4: Momentum exchange process

the MXER system to be worthwhile, however, it must have a cost-efficient way to regain the momentum transferred to the satellite. Because electrodynamic reboost requires only electrical power that comes from onboard solar panels, it offers the sustainability necessary to justify the expense of the MXER system.

One of the issues in electrodynamic tether propulsion is generating the electrical currents necessary to produce the boost forces. This requires the collection of electrons from the ionosphere, as well as their expulsion back to the ionosphere. While electron guns generally provide the electron emission, there are several possible ways to collect electrons. One of the simplest ways to do this is to use a positively biased spherical electron collector. An idea receiving more attention recently is to use a portion of the tether itself to collect electrons. Estes *et al.* did a study highlighting the mass and power savings possible by using a bare tether to collect electrons [7]. Estes, Sanmartín, and Martínez-Sánchez analyzed the performance of bare tether electron collection under varying environmental conditions. They found that bare tethers can collect current in a more efficient regime than spherical conductors. Bare tethers also have self-regulating characteristics which make them relatively insensitive to variations in ionospheric plasma density [8].

1.2.1 Stability Analyses of Electrodynamic Tethers

The complicated interactions inherent in electrodynamic tether operation give rise to equally complicated questions of their stability. Peláez and Andres investigated the stability of inert, hanging tethers in inclined, elliptical orbits. They found that, because the local vertical in elliptical orbits does not rotate uniformly, a hanging tether will not have a naturally stable equilibrium point. Instead, it will have families of periodic solutions. Peláez and Andres characterized the stability of these equilibrium solutions based on orbital inclination and eccentricity [18].

Somenzi, Iess, and Peláez performed a linear stability analysis of electrodynamic tethers in inclined, circular orbits. While they used a less complicated, linear approximation of the tether dynamics, they employed very accurate models of the Earth's geomagnetic field to shed light on some of the causes of instability in electrodynamic tethers. They found that

variations in ionospheric density and the geomagnetic field in inclined orbits add harmonic forcing terms that resonate with both librational and vibrational modes, causing instability. Coupling of the in- and out-of-plane dynamics further complicate the dynamics [35].

1.2.2 Control of Tethered Space Systems

Much work has been done developing possible strategies for the control of tethered spacecraft. Kojima *et al.* developed a method of controlling tether angles in a three-mass tethered system. The tethers were treated as rigid and massless, and differential geometry and delayed feedback chaos control were used to stabilize libration in the system [14]. Williams *et al.* investigated using electrodynamic Lorentz forces along with a movable attachment point to reduce string vibrations in a hanging tether simulation. They proposed using wave-absorbing boundary control at the attachment point to reduce the magnitude of traveling waves along the tether [44]. Mankala and Agrawal proposed the use of a variable resistor as a control actuator for electrodynamic tethers. They consider tethers in circular, equatorial orbits, and develop a feedback control algorithm for equilibrium-to-equilibrium librational moves [17]. Tragesser and San used the general perturbation equations to develop analytical current control laws for orbital maneuvering of electrodynamic tethered satellites. They ignore flexible tether dynamics completely, assuming the tether to be rigid, massless, and in a constant, hanging orientation. So, while coupling between orbital parameters is taken into effect, tether libration effects are ignored [39]. In 2005, Paul Williams expanded on this work to include tether libration effects. He showed that properly utilizing tether librations can increase the efficiency of orbital transfers by directing more of the electromagnetic force in the direction of orbit boosting [42].

The next chapter presents a new command shaping algorithm for reducing residual vibration in tower cranes. After command shaping has proven effective on this nonlinear Earth-based cable system, it is applied to flexible electrodynamic tethers. Chapter 3 investigates flexible tether dynamics within a constant orbit, and Chapter 4 extends the investigation to the case of orbit boosting.

CHAPTER II

COMMAND SHAPING FOR NONLINEAR TOWER CRANE DYNAMICS

To demonstrate the efficacy of input shaping on nonlinear systems, we first look at nonlinear crane dynamics. Cranes are an ideal setup for implementing input shaping because they are very lightly damped systems that will continue to oscillate long after the desired move has ended. Unfortunately, input shaping relies on superposition, and, since the equations of motion for all cranes are inherently nonlinear, the reliance on superposition is not appropriate for all operating regimes.

This chapter investigates two types of cranes, a bridge crane and a tower crane. Nonlinear equations of motion are presented and then verified using a portable bridge crane [16] at Georgia Tech and a portable tower crane [15] at Tokyo Tech. These equations are then linearized and the transition from predominantly linear to substantially nonlinear behavior is investigated for the bridge crane. The effectiveness of traditional input shaping on bridge cranes is explained, and a novel command shaping algorithm is proposed for dealing with nonlinear tower crane dynamics.

2.1 Bridge Crane

2.1.1 System Model

An illustration of a bridge crane is shown in Figure 5. A picture of the portable bridge crane used for experiments is shown in Figure 6. The trolley slides along the bridge in the x direction, and the bridge moves along the runway in the y direction. Thus, the trolley naturally operates in a Cartesian space. If the suspension length, L, is held constant, then the equations of motion relating the payload swing angles ϕ and θ to the acceleration of the

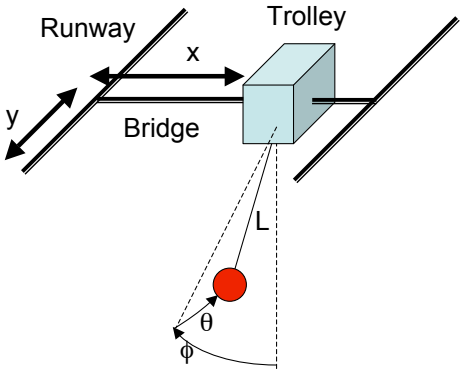

Figure 5: Bridge crane schematic.

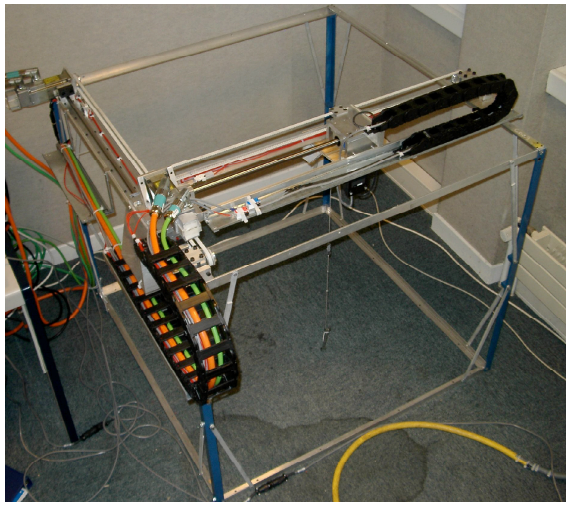

Figure 6: Picture of portable bridge crane.

trolley in the x and y directions are [4]:

$$\begin{aligned} L\ddot{\phi} + L\dot{\theta}^2 \cos(\phi)\sin(\phi) + g\sin(\phi)\cos(\theta) &= \ddot{x}\cos(\phi) + \ddot{y}\sin(\phi)\sin(\theta)\ , \\ L\ddot{\theta}\cos(\phi) - 2L\dot{\phi}\dot{\theta}\sin(\phi) + g\sin(\phi) &= -\ddot{y}\cos(\theta)\ . \end{aligned} \tag{9}$$

These equations can be converted into nonlinear state space equations of the form

$$\dot{\vec{x}} = f(\vec{x}, \vec{u})\ , \tag{10}$$

where

$$\begin{aligned} \vec{x} &= \begin{bmatrix} \phi & \dot{\phi} & \theta & \dot{\theta} & x & \dot{x} & y & \dot{y} \end{bmatrix}^T\ , \\ \vec{u} &= \begin{bmatrix} \ddot{x} & \ddot{y} \end{bmatrix}^T\ . \end{aligned} \tag{11}$$

This yields the following state space equations

$$\begin{aligned} \dot{x_1} &= x_2 \\ \dot{x_2} &= -x_4^2\cos(x_1)\sin(x_1) - \frac{g}{L}\sin(x_1)\cos(x_3) + \frac{1}{L}u_1\cos(x_1) + \frac{1}{L}u_2\sin(x_1)\sin(x_3) \\ \dot{x_3} &= x_4 \\ \dot{x_4} &= 2x_2x_4\tan(x_1) - \frac{g}{L}\frac{\sin(x_3)}{\cos(x_1)} - \frac{1}{L}u_2\frac{\cos(x_3)}{\cos(x_1)} \\ \dot{x_5} &= x_6 \qquad \dot{x_6} = u_1 \qquad \dot{x_7} = x_8 \qquad \dot{x_8} = u_2 \end{aligned} \tag{12}$$

In order to obtain a linear model of the system, the system can be linearized about $\vec{x} = \vec{u} = \vec{0}$ according to the following formula

$$A = \left[\begin{array}{cccc} \frac{\partial f_1}{\partial x_1} & \frac{\partial f_1}{\partial x_2} & \cdots & \frac{\partial f_1}{\partial x_n} \\ \frac{\partial f_2}{\partial x_1} & \frac{\partial f_2}{\partial x_2} & & \vdots \\ \vdots & & \ddots & \vdots \\ \frac{\partial f_n}{\partial x_1} & \cdots & \cdots & \frac{\partial f_n}{\partial x_n} \end{array} \right]_{\vec{x}=\vec{0}} \quad B = \left[\begin{array}{cccc} \frac{\partial f_1}{\partial u_1} & \frac{\partial f_1}{\partial u_2} & \cdots & \frac{\partial f_1}{\partial u_m} \\ \frac{\partial f_2}{\partial u_1} & \frac{\partial f_2}{\partial u_2} & & \vdots \\ \vdots & & \ddots & \\ \frac{\partial f_n}{\partial u_1} & \cdots & & \frac{\partial f_n}{\partial u_m} \end{array} \right]_{\vec{u}=\vec{0}} \tag{13}$$

to obtain the following linear state space equation

$$\dot{\vec{x}} = A\vec{x} + B\vec{u} \tag{14}$$

where

$$A = \left[\begin{array}{cccccccc} 0 & 1 & 0 & 0 & 0 & 0 & 0 & 0 \\ -\frac{g}{L} & 0 & 0 & 0 & 0 & 0 & 0 & 0 \\ 0 & 0 & 0 & 1 & 0 & 0 & 0 & 0 \\ 0 & 0 & -\frac{g}{L} & 0 & 0 & 0 & 0 & 0 \\ 0 & 0 & 0 & 0 & 0 & 1 & 0 & 0 \\ 0 & 0 & 0 & 0 & 0 & 0 & 0 & 0 \\ 0 & 0 & 0 & 0 & 0 & 0 & 0 & 1 \\ 0 & 0 & 0 & 0 & 0 & 0 & 0 & 0 \end{array} \right] \quad B = \left[\begin{array}{cc} 0 & 0 \\ \frac{1}{L} & 0 \\ 0 & 0 \\ 0 & \frac{1}{L} \\ 0 & 0 \\ 1 & 0 \\ 0 & 0 \\ 0 & 1 \end{array} \right] \tag{15}$$

The payload position is given by

$$x_{payload} = x - L\sin(\phi) \quad y_{payload} = y + L\cos(\phi)\sin(\theta) \tag{16}$$

2.1.2 Model Verification

The portable bridge crane used for model verification is approximately 1 m^3 in size. It is driven by two Siemens synchronous AC servo motors that move the trolley and bridge axes via timing belts, allowing movement in the x and y directions. A Siemens digital camera is attached to the trolley to measure the payload swing, and a Siemens programmable logic controller (PLC) is used to generate the velocity commands. These commands are sent to the motor drives which use encoders for Proportional-plus-Integral (PI) velocity feedback control [16].

Under normal operation, the payload swing angles are fairly small, thereby causing bridge cranes to behave in a linear manner. Figure 7 shows an overhead view of the *nonlinearly* simulated and measured crane payload responses to a typical two-axis move, while Figure 8 shows the *linearly* simulated response. Comparing Figures 7 and 8 shows that the nonlinear and linear models have nearly identical responses for small payload swing angles. To accentuate the model differences and to verify the nonlinear equations of motion, a trajectory that induces large swing angles and velocities was used to drive both the numerical simulations and the portable bridge crane. The trolley was driven close to the natural frequency of vibration on one axis to induce large swing angles. Then, at the approximate time of maximum swing on one axis, the crane was driven in the transverse direction, essentially creating large initial conditions for a transverse move. Figures 9 and 10 show overhead views of the simulated and measured crane responses. Figure 9 shows fairly good agreement between the experimental data and the nonlinear simulation. The response of the linear model is graphed with the experimental response in Figure 10. The large difference seen between the two models is apparent in the coupling between the two swing angles. This is evident in the swirling effect seen in the experimental and nonlinear data, but which is absent from the linear model. Further comparison can be made by graphing the payload swing angles individually. These profiles can be seen in Figures 11 and 12. The linear model predicts a constant amplitude in the θ and ϕ directions, while the nonlinear model shows transfer of vibration from the ϕ to the θ direction. This transfer is

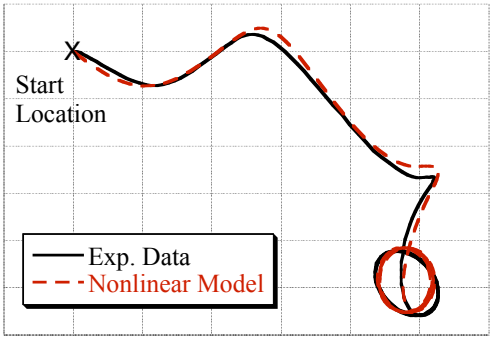

Figure 7: Experimental and nonlinearly simulated payload trajectories.

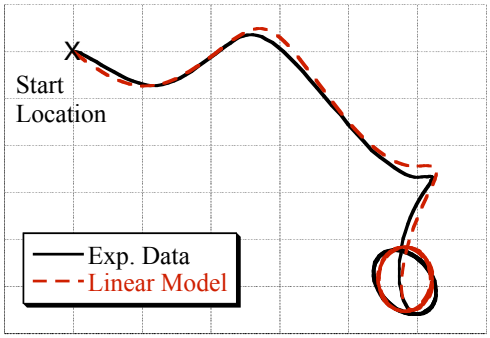

Figure 8: Experimental and linearly simulated payload trajectories.

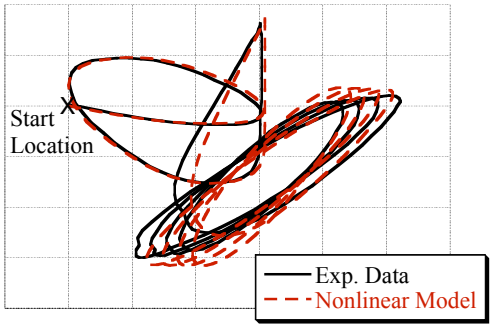

Figure 9: Experimental and nonlinearly simulated payload trajectories.

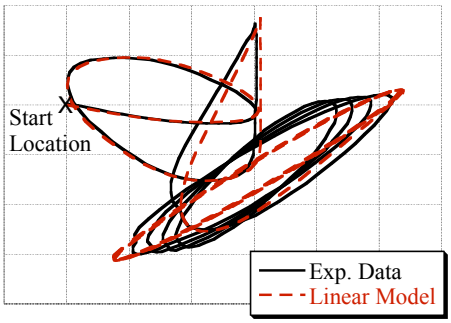

Figure 10: Experimental and linearly simulated payload trajectories.

evident in the experimental data of Figure 11. Figure 12 shows the nonlinear θ vibration growing slightly as energy is transferred from the ϕ direction. The linear vibration stays the same, as is expected, but the experimental vibration amplitude decreases with time. This is most likely due to aerodynamic damping in the real system that is unaccounted for in either of the dynamic models. The experimental behavior is close to the nonlinear predictions, and, for the extreme motions seen in this example, the nonlinear model shows a clear advantage over the linear model.

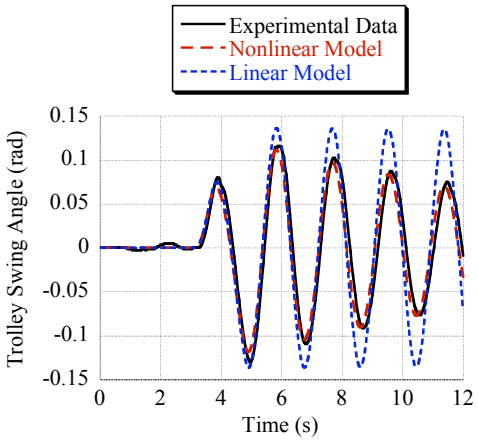

Figure 11: Experimental and simulated trolley swing angle (ϕ).

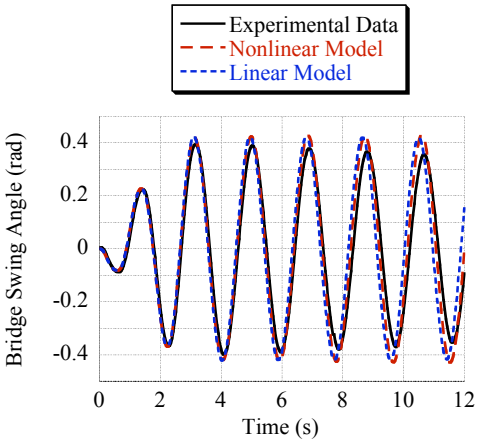

Figure 12: Experimental and simulated bridge swing angle (θ).

2.1.3 Nonlinear Transition

There are two assumptions that transform the nonlinear crane equations, (9), to the linearized model:

$$\ddot{\phi} = -\frac{g}{L}\phi + \frac{1}{L}\ddot{x}\,, \quad \ddot{\theta} = -\frac{g}{L}\theta + \frac{1}{L}\ddot{y}\,. \tag{17}$$

The first assumption is that the payload angular velocity is small: $\left[\dot{\phi}, \dot{\theta}\right] \ll 1$. Because these terms appear as second-order terms in (9), they are neglected. The second assumption is that the angular deflection is small: $[\phi, \theta] \ll 1$. Using the small angle approximations for sine and cosine yields the linearized model, which in turn yields a linear approximation of the oscillation period. As these swing angles increase, the nonlinear period of oscillation changes, as seen in Figure 13. These changes are small. For example, there is only a 5% difference at a swing angle of 50°.

In most real crane operations, large swing angles and velocities are neither safe nor useful. For most reasonable operating regimes (including the working range of the portable bridge crane), the swing angles and velocities are small enough that there is virtually no difference between the linear and nonlinear models. Because of this, input shaping has been shown to be very effective on bridge cranes [9, 22, 37]. In fact, input shaping further suppresses the swing angles, thereby keeping the crane operating in the linear regime and improving its own effectiveness.

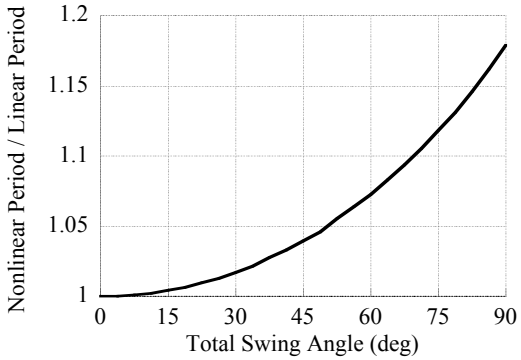

Figure 13: Ratio of nonlinear to linear oscillation periods.

2.2 Tower Crane

2.2.1 System Model

An illustration of a tower crane is shown in Figure 14. The trolley slides along the boom in the R direction, and the boom rotates around the mast in the s direction. If the suspension length is constant, then the equations of motion relating the payload swing angles ϕ and θ to the motion of the trolley in the R and s directions are [4]:

$$\begin{aligned} L\ddot{\phi} + L\dot{\theta}^2 \cos(\phi)\sin(\phi) + g\sin(\phi)\cos(\theta) &= -\ddot{R}\cos(\phi) + R\dot{s}^2\cos(\phi) \\ &\quad -R\ddot{s}\sin(\phi)\sin(\theta) - 2\dot{R}\dot{s}\sin(\phi)\sin(\theta) \\ &\quad -2L\dot{s}\dot{\theta}\cos^2(\phi)\cos(\theta) - L\ddot{s}\sin(\theta) \\ &\quad +L\dot{s}^2\sin(\phi)\cos^2(\theta)\cos(\phi)\ , \\ L\ddot{\theta}\cos(\phi) - 2L\dot{\phi}\dot{\theta}\sin(\phi) + g\sin(\theta) &= R\ddot{s}\cos(\theta) + 2\dot{R}\dot{s}\cos(\theta) + 2L\dot{s}\dot{\phi}\cos(\phi)\cos(\theta) \\ &\quad +L\ddot{s}\sin(\phi)\cos(\theta) + L\dot{s}^2\sin(\theta)\cos(\phi)\cos(\theta)\ . \end{aligned} \tag{18}$$

With state space variables

$$\begin{aligned} \vec{x} &= \begin{bmatrix} \phi & \dot{\phi} & \theta & \dot{\theta} & R & \dot{R} & s & \dot{s} & L & \dot{L} \end{bmatrix}^T\ , \\ \vec{u} &= \begin{bmatrix} \ddot{R} & \ddot{s} & \ddot{L} \end{bmatrix}^T\ , \end{aligned} \tag{19}$$

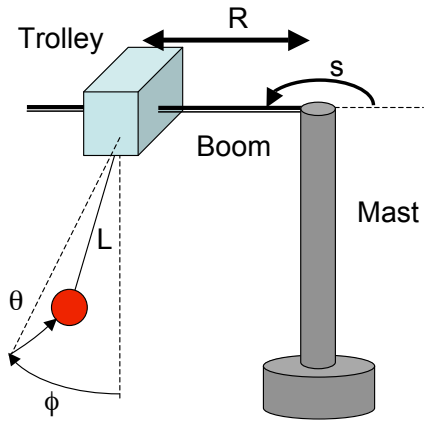

Figure 14: Tower crane schematic.

we find the nonlinear state space equations

$$
\begin{aligned}
&\dot{x_1} = x_2 \\
&\dot{x_2} = -x_4^2 \cos(x_1)\sin(x_1) - 2x_8x_4\cos^2(x_1)\cos(x_3) - u_2\sin(x_3) + x_8^2\sin(x_1)\cos^2(x_3)\cos(x_1) \\
&+\frac{1}{x_9}\left(-g\sin(x_1)\cos(x_3) - u_1\cos(x_1) + x_5x_8^2\cos(x_1) - x_5u_2\sin(x_1)\sin(x_3) - 2x_6x_8\sin(x_1)\sin(x_3)\right) \\
&\dot{x_3} = x_4 \\
&\dot{x_4} = 2x_2x_4\tan(x_1) + \cos(x_3)\left(2x_8x_2 + u_2\tan(x_1) + x_8^2\sin(x_3)\right) \\
&+\frac{1}{x_9\cos(x_1)}\left(-g\sin(x_3) + x_5u_2\cos(x_3) + 2x_6x_8\cos(x_3)\right) \\
&\dot{x_5} = x_6 \qquad \dot{x_6} = u_1 \qquad \dot{x_7} = x_8 \qquad \dot{x_8} = u_2 \qquad \dot{x_9} = x_{10} \qquad \dot{x_{10}} = u_3\,.
\end{aligned}
\tag{20}
$$

Assuming a constant length, L_0, and partially linearizing these states using (13) and (14), we obtain

$$
A_{twr} = \begin{bmatrix}
0 & 1 & 0 & 0 & 0 & 0 & 0 & 0 \\
-\frac{g}{L_0} & 0 & 0 & 0 & 0 & 0 & 0 & 0 \\
0 & 0 & 0 & 1 & 0 & 0 & 0 & 0 \\
0 & 0 & -\frac{g}{L_0} & 0 & 0 & 0 & 0 & 0 \\
0 & 0 & 0 & 0 & 0 & 1 & 0 & 0 \\
0 & 0 & 0 & 0 & 0 & 0 & 0 & 0 \\
0 & 0 & 0 & 0 & 0 & 0 & 0 & 1 \\
0 & 0 & 0 & 0 & 0 & 0 & 0 & 0
\end{bmatrix}
\quad
B_{twr} = \begin{bmatrix}
0 & 0 \\
-\frac{1}{L_0} & 0 \\
0 & 0 \\
0 & \frac{R}{L_0} \\
0 & 0 \\
1 & 0 \\
0 & 0 \\
0 & 1
\end{bmatrix}
\tag{21}
$$

This linearization technique yields only quasi-linear matrices, with B_{twr} depending on R. It was decided to linearize about a constant cable length and ignore hoisting in this linearization while keeping some of the dependence of the dynamics on R. This method ignores dynamic effects in R while allowing the instantaneous R to influence the swing angles. The resulting quasi-linear system captures the cylindrical motion inherent in the system. For both the linear and the nonlinear models, the payload position is given by

$$
\begin{aligned}
x_{payload} &= [R + L\sin(\phi)]\cos(s) + [L\sin(\theta)\cos(\phi)]\sin(s) \\
y_{payload} &= [R + L\sin(\phi)]\sin(s) - [L\sin(\theta)\cos(\phi)]\cos(s)
\end{aligned}
\tag{22}
$$

2.2.2 Model Verification

A sketch of the tower crane used for experimental verification is shown in Figure 15, and a picture is shown in Figure 16. The crane is approximately 2 m tall with a 1 m boom

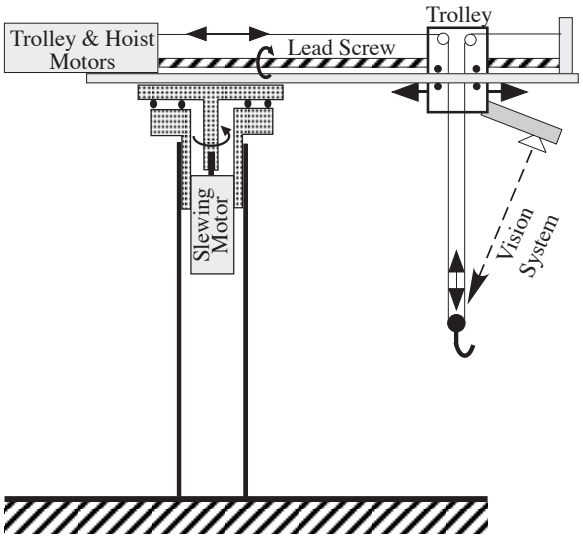

Figure 15: Schematic layout of tower crane.

Figure 16: Picture of portable tower crane.

arm. The crane has 3 degrees of freedom actuated by Siemens synchronous AC servo motors. The slewing motor controls the rotation axis, which is capable of 340° rotation. The trolley moves radially via a lead screw, and the hoisting motor controls the suspension cable length. In addition, a Siemens digital camera is mounted to the trolley and records the swing deflection of the payload at a rate of 25 Hz. A Siemens PLC sends velocity setpoints to Siemens Sinamic motor drives, which use motor encoder signals to provide PI velocity feedback control [15].

Because the tower crane exhibits noticeable nonlinear behavior for nearly all moves, realistic moves were performed and compared with the simulated responses. Figures 17 and 18 show the responses for a combined slew and radial move. As can be seen, the nonlinear simulations in Figure 17 predict crane behavior fairly well, while the linear model ignores all coupling between radial and tangential motion. The deflection angles are also similar for the nonlinear model and experimental data, as can be seen in Figures 19 and 20. Figure 19 shows that the crane exhibits significant damping in the radial direction. This is because of the configuration of the payload cable, as seen in Figure 15. To allow hoisting and radial motion of the trolley, the payload cable runs through a pulley on one side of the trolley.

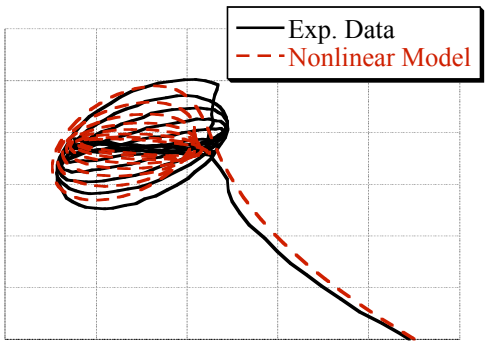

Figure 17: Experimental and nonlinearly simulated payload trajectories.

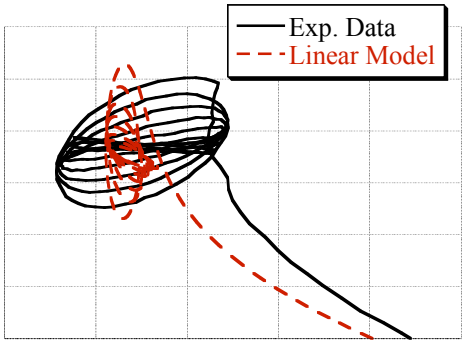

Figure 18: Experimental and linearly simulated payload trajectories.

It then goes down to meet a pulley on the payload and back up to a second pulley on the opposite side of the trolley. These pulleys allow the trolley to move along the boom while keeping a constant payload length. This configuration means that any radial vibration will cause the pulleys on the trolley to rotate, which leads to friction damping. In order to achieve better agreement with the experimental data, viscous damping was added to the original models.

2.2.3 Input Shapers

In order to improve the performance of input shaping, we endeavor to design an input shaper to deal with the specific nonlinearities associated with slewing motions of tower cranes. As

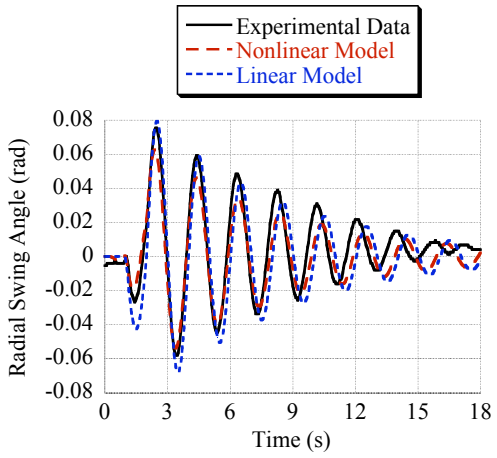

Figure 19: Experimental and simulated radial swing angle (ϕ).

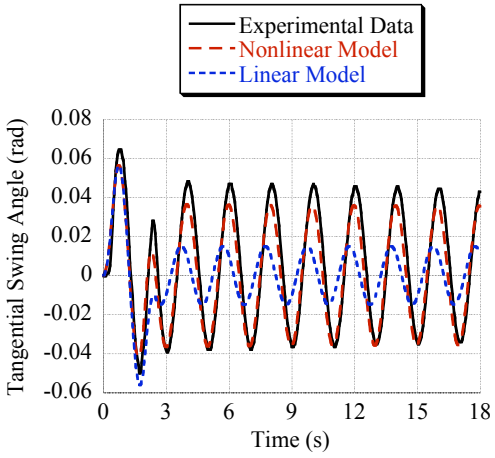

Figure 20: Experimental and simulated tangential swing angle (θ).

the boom rotates, the payload tends to swing outward in the radial direction due to a lack of sufficient centripetal force. When the move is completed, the payload will then vibrate in the radial direction. Also, from (18), we see that there are inherent interactions that cause the rotational and radial velocities to affect both swing angles.

To investigate these effects, we simulated a rotational move with a trapezoidal slewing velocity profile. A trapezoidal slewing velocity profile drives the crane through a circular rest-to-rest slewing motion. Figure 21 shows an overhead view of the move, and Figure 22 shows the radial and tangential swing angles during the move. The swing angles show two dominant frequencies: the 0.5 Hz natural frequency corresponding to classical pendulum motion and another related to the angular velocity of the boom by

$$\pi = T\psi \tag{23}$$

where ψ is the angular velocity of the boom and T is the period. If we look at the low-frequency envelope functions that bound the vibration, then the envelope function for the radial swing angle is very nearly 90° out of phase with that of the tangential swing angle. We conclude that this is due to the transfer of momentum from the radial to tangential directions as the payload moves through 90° of rotation. That is, once the boom has rotated 90°, the original orientations of the radial and tangential directions have now exactly switched: the radial direction is now in the original tangential direction, and vice versa. This seems to indicate that a conservation of linear momentum effect is more dominant than nonlinear

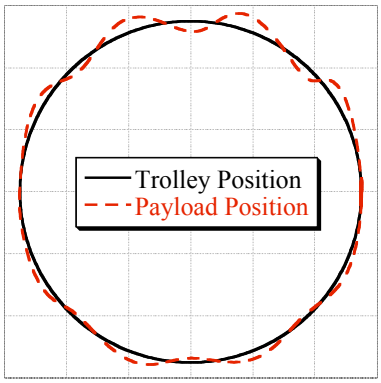

Figure 21: Unshaped slew of tower crane.

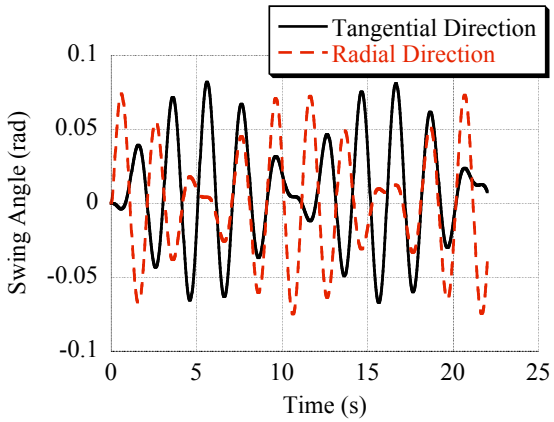

Figure 22: Swing angles during unshaped slew.

interactions in the equations of motion.

A traditional ZV shaper convolved with a slewing profile will yield two accelerations in the tangential direction, as shown by the arrows in Figure 23. However, due to the rotational nature of the tower crane, these accelerations are no longer in the same direction; the second acceleration has been rotated through an angle of Δs. This effect degrades the performance of traditional input shapers.

The importance of momentum effects lead us to consider the advanced input shaper illustrated in Figure 24. This input shaper is designed for a pure rotational move. In order to better cancel the vibration induced by the first impulse, we would like the second impulse to act in the same direction as the first impulse. This leads us to add radial components to the slewing motion to achieve the same resultant direction for both impulses, as seen in Figure 24. By letting

$$\begin{aligned} A_2 &= \cos(\Delta s) \\ B_2 &= \sin(\Delta s) \end{aligned} \tag{24}$$

we get a resultant vector, $\vec{V}_2$, that acts in the same direction as the first impulse, allowing more of the vibration to be cancelled. This directional alignment approach is the general design method for the advanced slewing shaper.

In order to justify this directional approach, it is necessary to determine whether or not induced vibration is influenced by slewing motion of the crane. To do this, two moves were

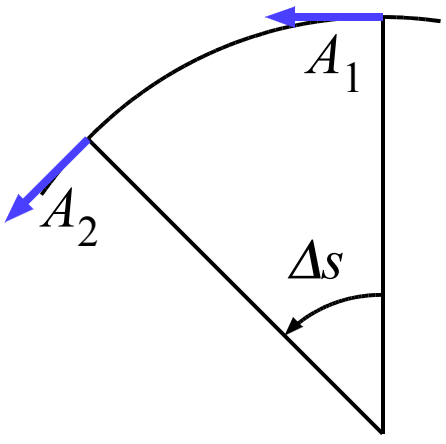

Figure 23: Traditional ZV shaping.

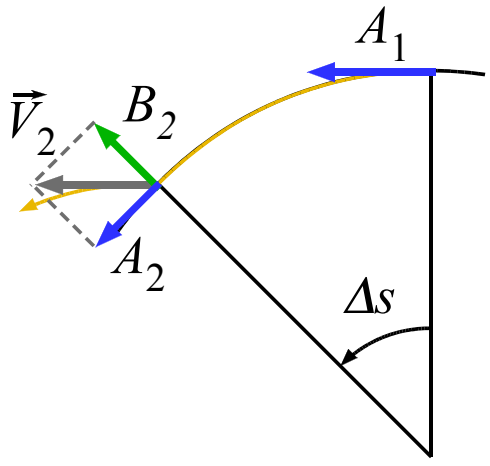

Figure 24: Schematic for slewing input shaper.

performed and compared. The crane was moved through a slew both with and without initial swing of the payload. The zero initial conditions response was then subtracted from the full response to determine the effect of the move on the initial vibration. As can be seen in Figure 25, the orientation of the original vibration remains nearly unchanged.

In attempting to implement the advanced shaper, we run into several challenges. The most significant is the fact that adding a single impulse in the radial direction causes a nonzero radial velocity during the entire move. By ignoring this effect, we are able to suppress the swing angles, but it leads to significant radial drift, as seen in Figure 26. Therefore, we must improve on this approach and attempt to give an inward impulse followed by an equal magnitude outward impulse in the radial direction, as illustrated in Figure 27. The resulting motion will have no radial velocity during the constant velocity portion of the slew.

The shaper will consist of two sets of impulses, one for angular motions, and one for radial motions. This is represented as:

$$\begin{bmatrix} A_i \\ t_i \end{bmatrix} = \begin{bmatrix} \gamma_1 & \gamma_2 \\ 0 & T/2 \end{bmatrix} \quad \begin{bmatrix} B_i \\ t_i \end{bmatrix} = \begin{bmatrix} -\delta_1 & \delta_1 \\ 0 & T/2 \end{bmatrix} \tag{25}$$

where A_i are the impulse amplitudes in the slewing direction, B_i are those in the radial

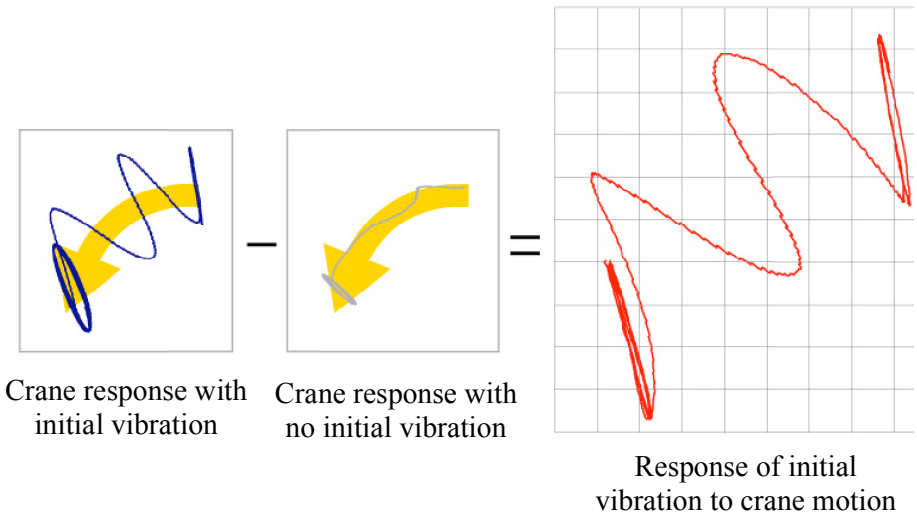

Figure 25: Effect of slew on initial vibration.

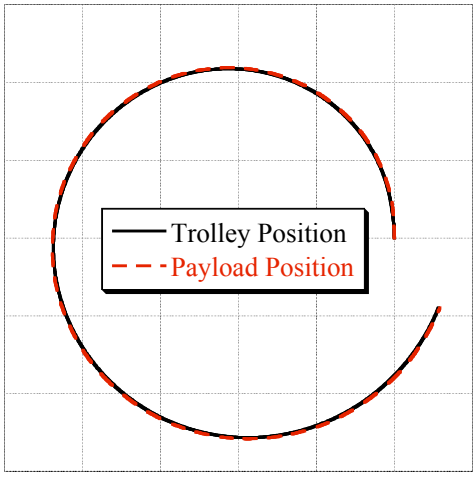

Figure 26: Slew of tower crane with non-linear slewing shaper.

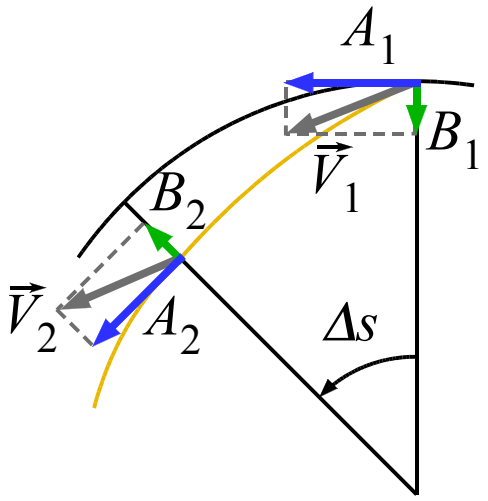

Figure 27: Improved slewing shaper.

direction, and t_i are the impulse times. Setting $\vec{V}_1 = \vec{V}_2$ and constraining $\sum A_i = 1$ yields:

$$\gamma_1 + \gamma_2 = 1\,, \quad \delta_1 = \alpha\gamma_1 R_0\,, \quad \gamma_2\left(R_0 - \frac{\delta_1 \ddot{s}\, t_r}{2}\,(T - t_r)\right) = \beta\gamma_1 R_0 \tag{26}$$

where R_0 is the starting radial position of the trolley, $\ddot{s}$ is the acceleration of an assumed trapezoidal velocity profile with rise time, $t_r < T/2$, and:

$$\alpha = \frac{1}{[1 + \cos(\Delta s)]\cot(\Delta s) + \sin(\Delta s)}\,, \quad \beta = \alpha\,\frac{1 + \cos(\Delta s)}{\sin(\Delta s)}\,, \quad \Delta s = \frac{\gamma_1 \ddot{s}\, t_r}{2}\,(T - t_r) \tag{27}$$

Equations (26) and (27) can be solved for the three unknowns, γ_1, γ_2, and δ_1, using a standard nonlinear solver. This process is an easy numerical operation and only depends on three crane parameters, $\ddot{s}$, t_r, and R_0. Once the shapers are determined, they are both convolved with the angular velocity profile to obtain shaped velocity profiles for the radial and slewing directions. It is important to check that $\delta_1 \ddot{s}$ does not exceed the maximum acceleration in the radial direction, $\ddot{R}$.

To measure the effectiveness of this new command shaping process, we compare the final residual vibration for unshaped, ZV shaped, and ZVD shaped moves against a move created using the slewing shaper defined by (25). Figure 28 shows the performance of the three shapers compared to the unshaped case for $R_0 = 0.55$m, and $L_0 = 1$m. It is clearly evident that any form of input shaping is a vast improvement over the unshaped cases for nearly all move distances, even for very aggressive moves. Figures 29 and 30 show simulated

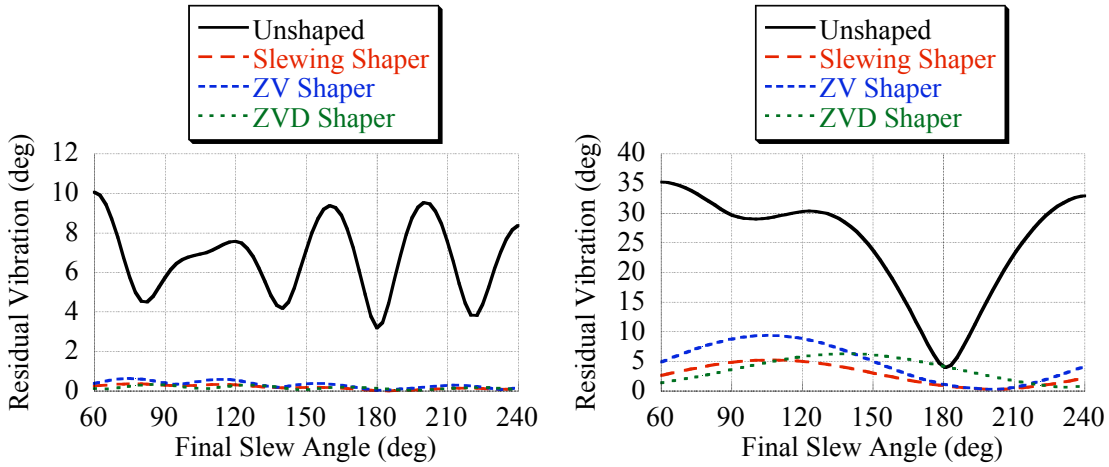

(a) $\ddot{s} = 40$ deg/s^2, $t_r = 0.5$ s (b) $\ddot{s} = 120$ deg/s^2, $t_r = 0.5$ s

Figure 28: Simulated unshaped and shaped residual vibration

residual vibration in the tangential and radial directions for various rotation angles and system parameters. For longer suspension lengths, the slewing shaper outperforms both ZV and ZVD shaping, while still having the same rise time as a ZV shaper. For shorter lengths, the slewing shaper performs better than a ZV shaper, but not as well as the ZVD shaper. Figures 31 and 32 show the corresponding experimental results. The experimental results show a similar trend, but the slewing shaper does not perform as well as the theory predicts in the radial direction. While this is not ideal, increased radial vibration is preferable to tangential vibration because of the inherent damping present in the radial direction. The increase in vibration is most likely due to the hardware being unable to track the radial command precisely. The radial velocity profiles have very small magnitudes, magnifying the error signal with respect to the desired velocity. Typical velocity errors seen in the experiments were $\pm 14\%$. To improve performance, the feedback gains used in the radial direction could have been optimized for slow velocities, but this modification was not performed.

To further investigate the influence of velocity tracking error on residual vibration, the system rise time was increased from $t_r = 0.5$ s to $t_r = 1.25$ s while keeping the acceleration constant. This takes the maximum slewing velocity, $\dot{s}_{max}$, from 20 deg/s to 50 deg/s. Figure 33 shows the simulation results for $R_0 = 0.9$ m and $L_0 = 1$ m. Even for these extreme speeds, input shaping is still able to drastically reduce the residual vibration. The

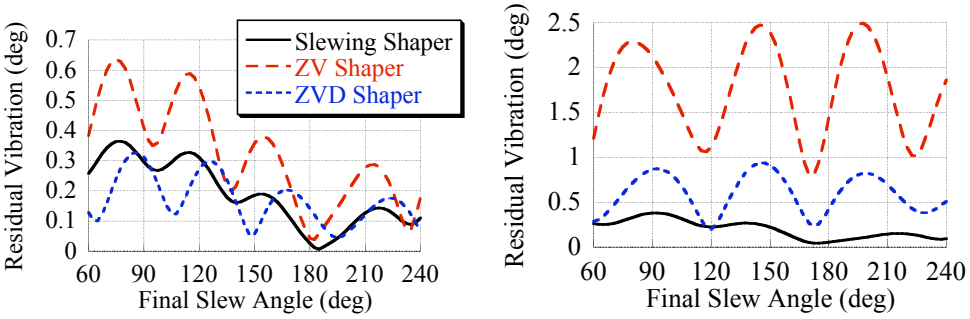

(a) $R_0 = 0.55$ m, $L_0 = 1$ m (b) $R_0 = 0.55$ m, $L_0 = 1.5$ m

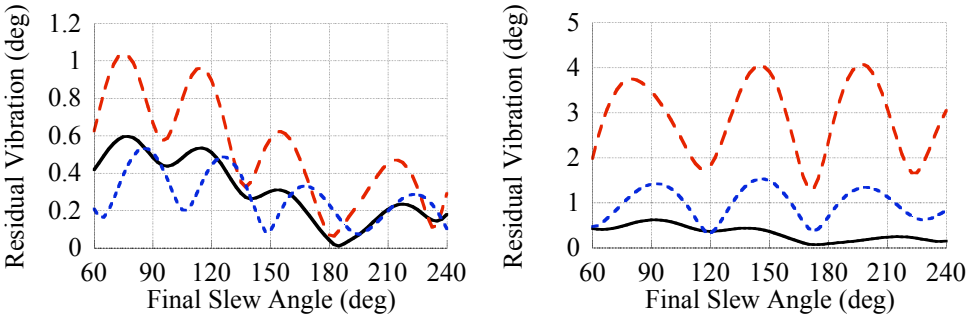

(c) $R_0 = 0.9$ m, $L_0 = 1$ m (d) $R_0 = 0.9$ m, $L_0 = 1.5$ m

Figure 29: Simulated residual vibration in the tangential direction

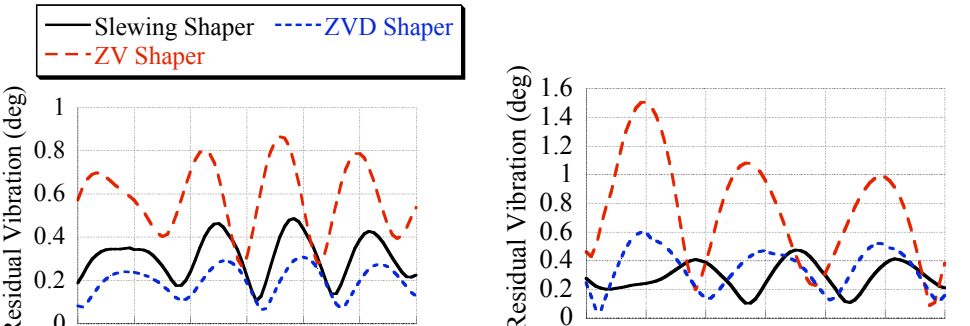

(a) $R_0 = 0.55$ m, $L_0 = 1$ m (b) $R_0 = 0.55$ m, $L_0 = 1.5$ m

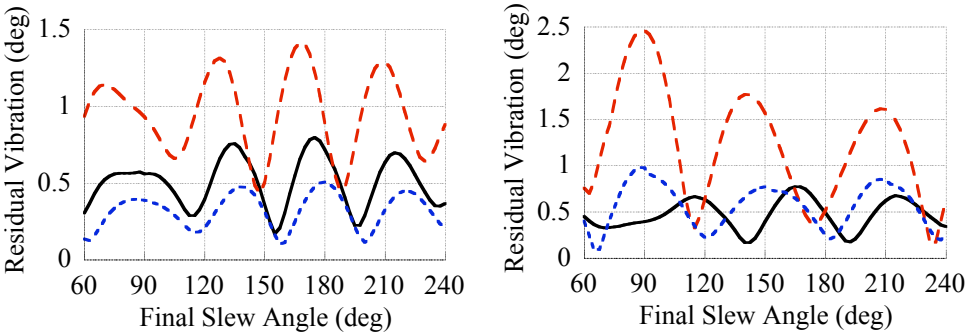

(c) $R_0 = 0.9$ m, $L_0 = 1$ m (d) $R_0 = 0.9$ m, $L_0 = 1.5$ m

Figure 30: Simulated residual vibration in the radial direction

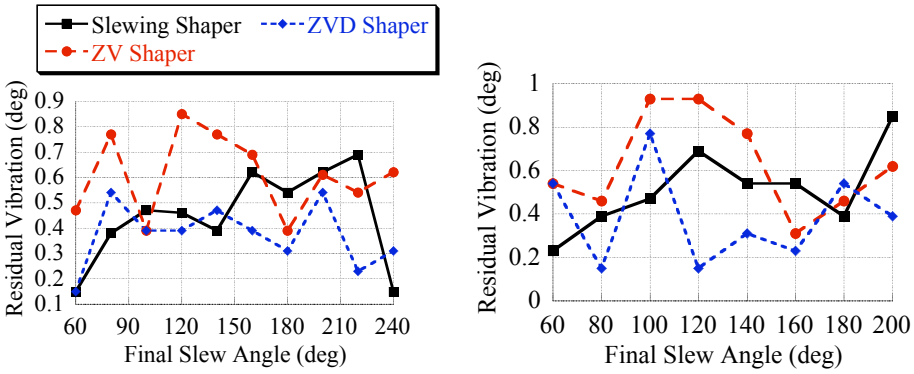

(a) $R_0 = 0.55$ m, $L_0 = 1$ m (b) $R_0 = 0.55$ m, $L_0 = 1.5$ m

(c) $R_0 = 0.9$ m, $L_0 = 1$ m (d) $R_0 = 0.9$ m, $L_0 = 1.5$ m

Figure 31: Experimental residual vibration in the tangential direction

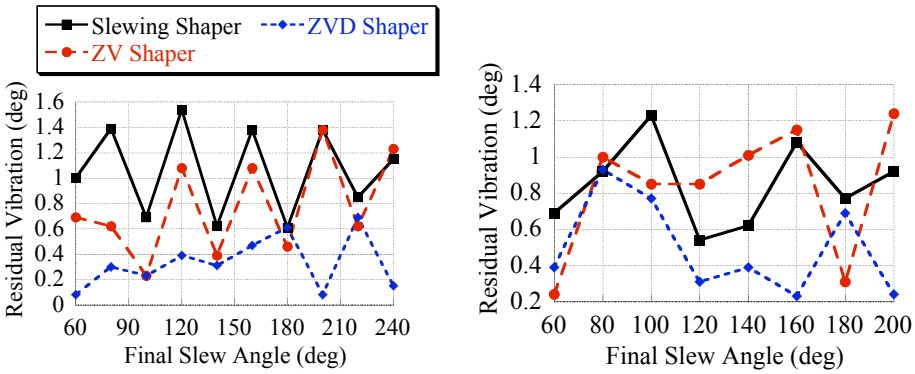

(a) $R_0 = 0.55$ m, $L_0 = 1$ m (b) $R_0 = 0.55$ m, $L_0 = 1.5$ m

(c) $R_0 = 0.9$ m, $L_0 = 1$ m (d) $R_0 = 0.9$ m, $L_0 = 1.5$ m

Figure 32: Experimental residual vibration in the radial direction

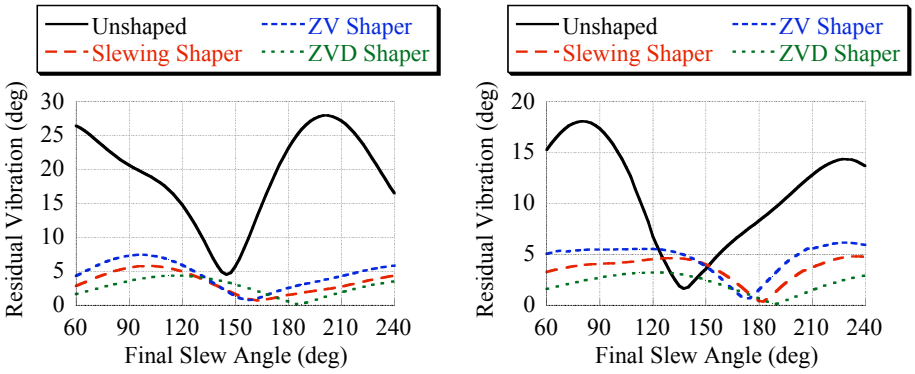

(a) Tangential vibration (b) Radial vibration

Figure 33: Simulated residual vibration, $\ddot{s} = 40$ deg/s^2, $t_r = 1.25$ s

slewing shaper vibration suppression is again in between that of the ZV and ZVD shapers. Figure 34 shows the corresponding experimental results. At these higher velocities, the relative error in the radial velocity is reduced, and the performance of the slewing shaper falls in between ZV and ZVD shaping, as expected.

2.3 Conclusions

Nonlinear equations of motion were presented for bridge and tower crane payload motion and verified experimentally. A novel command shaping algorithm based on nonlinear directional effects was presented for the slewing of tower cranes. Experimental results verify that the resulting shaper is more effective than traditional input shaping for reducing vibration in the direction of slewing motions. This advances the current state of input shaping technology

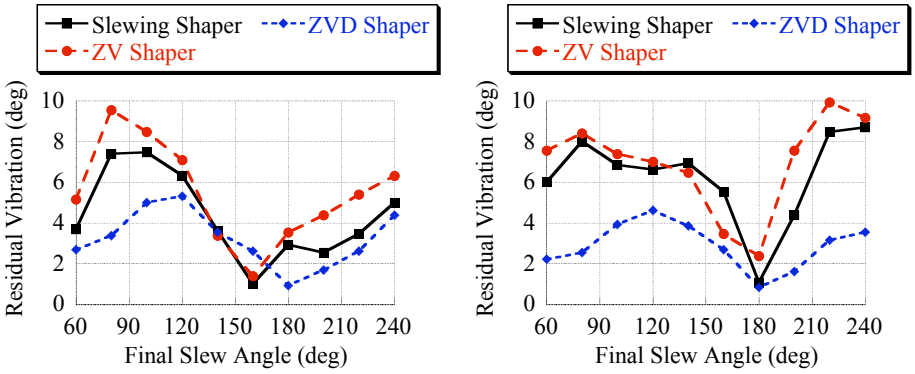

(a) Tangential vibration (b) Radial Vibration

Figure 34: Experimental residual vibration, $\ddot{s} = 40$ deg/s^2, $t_r = 1.25$ s

on nonlinear systems by improving vibration reduction and offering a new perspective on the problem of rotational motion. The vector design process used to create the advanced input shaper represents a new method of shaper design for tower cranes, and could also be extended to other input shaping applications that undergo similar transformations during motion.

CHAPTER III

INPUT SHAPING FOR CONSTANT-ORBIT FLEXIBLE TETHER DYNAMICS

Now that input shaping has been proven effective on an Earth-based nonlinear cable system, the problem of electrodynamic forces on long tethers in space is investigated. Passing a current through a long tether moving through the Earth's magnetic field produces a Lorentz force perpendicular to the magnetic field lines and to the line of the tether. If this force could be harnessed for satellite orbit boosting, it could reduce the need for refueling missions and increase the working lifetime of satellites. These tethers will exhibit large-scale oscillations that must be dealt with in order to make them a valid alternative to conventional thruster technology.

The system model used in this analysis was developed by Williams *et al.* [43] and consists of discrete masses connected by springs and dampers as illustrated in Figure 35. In this chapter, the orbit of the mother satellite is assumed to be constant, and flexible tether dynamics are investigated. This model is used because it is the simplest model that captures the primary flexible dynamics. As such, it offers the best starting point for the

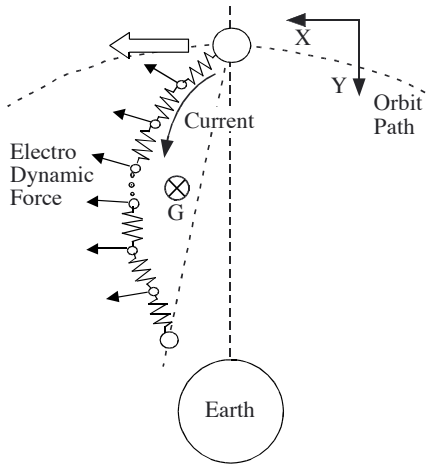

Figure 35: Model of electrodynamic tether propulsion

application of input shaping to this problem. A more complicated model will be examined in the following chapter. The MATLAB implementation of the equations of motion for this model is shown in Appendix A. The major shortcomings of the model are as follows:

- The orbit of the mother satellite is assumed constant, ignoring orbit boosting effects.
- The Earth's magnetic field is modeled as a dipole. A more sophisticated model would add harmonic excitations to the system. These excitations will depend on the orientation of the tether and the current applied.
- The Earth is treated as a point mass to determine gravity forces. Earth oblateness effects would add to the tether libration.
- Current collection dynamics are ignored. Changes in ionospheric electron density mean that some sort of control system will be necessary to produce the varying currents required by the input shaping controller.

When a step current is applied to the tether, it responds with large librations and string oscillations. These are evident as the two major frequency components seen in Figure 36. The low frequency oscillations represent pendulum-like librations of the tether while the high frequency oscillations are transverse string vibrations.

To lessen the unwanted dynamic effects in electrodynamic tethers, the electrical current sent through the tether must be intelligently controlled. If feedback control is relied upon

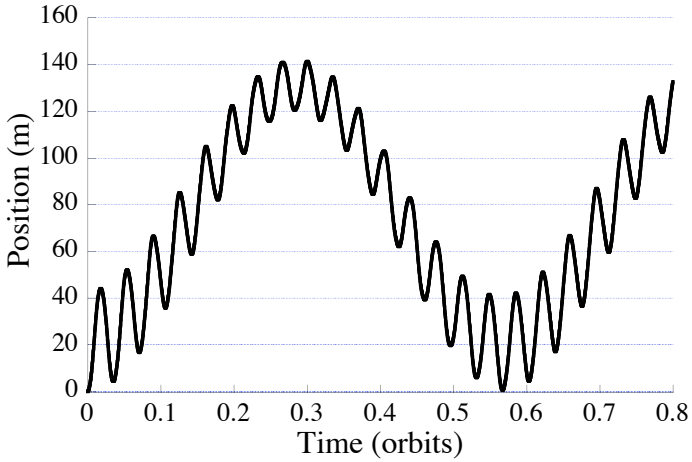

Figure 36: Tether midpoint response to step current input

for this effect, then numerous sensors will be required to measure the state of the tether. For many types of feedback control, an adequate state measurement may be unachievable. As an alternative control approach, input shaping can be applied to the current sent through the tether. This shapes the resulting thrust force so that vibration in the tether will be greatly reduced. As shown in Figure 36, tethers have two main modes of oscillation that must be addressed: 1) low frequency pendulum-like libration, and 2) numerous high frequency string-like modes.

3.1 Simulation and Input Shaping Results

Given the general qualities of the various input shapers described in the introduction and the needs of an electrodynamic tether, the approach advocated here is to use a UMZV shaper to reduce the libration. Because the libration frequency is fairly easy to estimate, it does not need the added robustness of a longer shaper. The UMZV shaper will also provide the fastest system rise time. In conjunction with this shaper, robust shapers (ZVD and EI) are employed to deal with the string vibration because these dynamics are a more complex function of tether length, line density, tension, and desired motion. Consequently, the input shapers addressing these phenomena need more robustness to possible parameter variations. These robust shapers also have the added benefit of reducing vibration in high frequencies that might otherwise be excited by the UMZV shaper.

3.1.1 Frequency Content Analysis

In order to properly apply input shaping, estimates of the natural frequencies and damping ratios must be known for each mode of vibration. It is important to note, though, that input shaping is based on linear estimations of the dynamics. The robustness inherent in some shapers helps them to reduce vibrations in the presence of system nonlinearities. Simulations of stationkeeping were conducted with nominal modeling parameter values set to the values in Table 1. The compressive damping factor is more important to the longitudinal dynamics of the tether than the transverse dynamics being studied here. Fast Fourier transforms (FFT's) were applied to the tether midpoint response (shown in Figure 36) to obtain frequency content data. To achieve higher resolution at the low frequencies

Table 1: Simulation parameters.

Simulation Parameter	Nominal Value
Tether Length, L	20 km
Tether Density, ρ	1 kg/km
Tether Stiffness, EA	10 kN
Subsatellite Mass, m_{subsat}	500 kg
Initial Orbital Altitude, H	200 km
Compressive Damping Factor c_{eq}	1.0

seen in this system, the simulations were run for a very long time, in this case 600000 seconds (approximately 100 orbits). From the FFT data, the periods of vibration were found to be 3061 seconds for the low frequency libration mode and 192 seconds for the high frequency string mode. The long simulation time yields a low FFT uncertainty of approximately 0.001% for the libration mode and 0.00006% for the string vibration mode. However, this is only the uncertainty that comes from the Fourier transform. System parameter uncertainty and unmodeled dynamics play a larger role in the uncertainty of the dynamic response. Damping is always small, and it is assumed to be zero for the purposes of input shaper design.

3.1.2 Input Shaping Performance

Once the frequencies have been adequately approximated, input shaping can be applied to the electrical current input. The solid line in Figure 37 shows that if the current is simply turned on, then the center of the tether deflects up to 140 m, and significant amounts of both libration and string vibration are induced in the system response. If the current is shaped using a ZVD shaper designed to suppress the first mode of string vibration, then the high-mode vibration is significantly reduced, as shown by the dashed line in Figure 37. What remains is essentially the libration mode that must be addressed with an additional shaper. If a UMZV shaper designed to suppress the libration is convolved with the ZVD shaper, then nearly all of the oscillation dynamics are eliminated, as shown by the dotted line in Figure 37. Note that the cost of this improvement is a 45% increase in the rise time of the tether response.

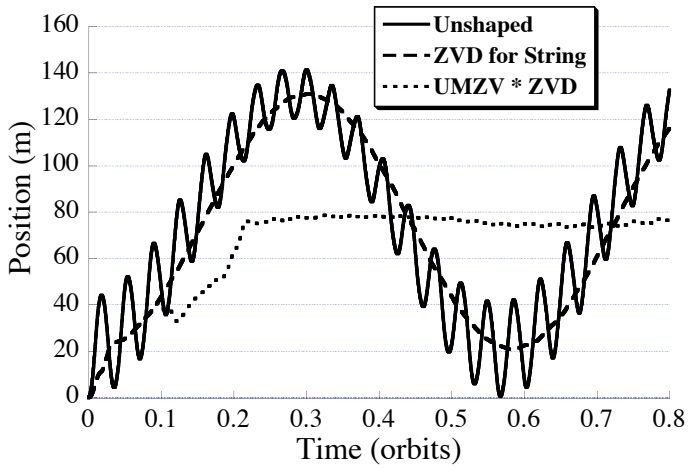

Figure 37: Displacement of tether midpoint

One of the major problems caused by the libration and string vibration is increased tension throughout the tether and at the connections to the main satellite and the subsatellite or payload. Figure 38 shows that input shaping greatly reduces the high-frequency tension oscillations experienced by the main satellite. Figure 39 shows that similar reductions in tension also occur at the subsatellite connection.

For the previous simulations, 10 node masses were used to model the flexible tether. In order to establish that 10 nodes are adequate to capture the dominant dynamic effects, the model complexity was increased. Figure 40 shows the displacement of the tether midpoint when the number of node masses is 10, 14, and 20. The tether response is very similar for the three cases shown. Because only a small improvement in fidelity is gained, at the cost of large increases in simulation time, a 10-node-mass tether is used for the remainder of this

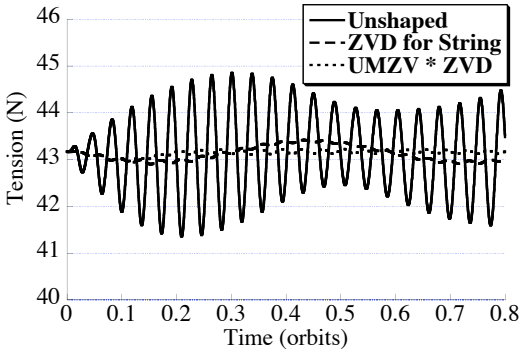

Figure 38: Tension at main satellite

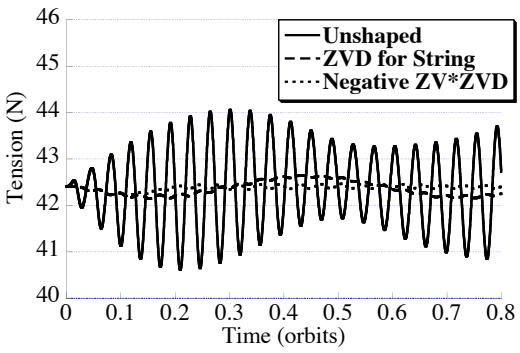

Figure 39: Tension at subsatellite

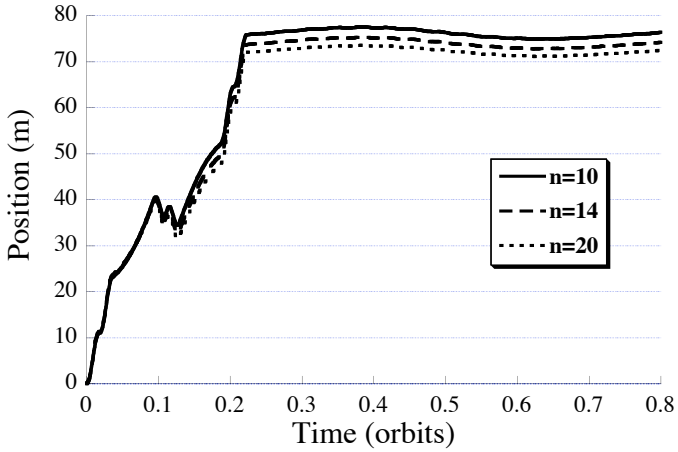

Figure 40: Displacement of tether midpoint for varying complexity of model

analysis.

3.1.3 Deflection-Limiting Current Profiles

While traditional input shapers successfully reduce residual oscillation, they may not substantially reduce high levels of transient deflection in the tether. As shown in Figure 37, even when the vibration is greatly reduced, there can still be a large steady-state deflection of the tether when the current is being applied. In this instance, the tether deflection gives a measure of the tether in-plane libration angle. It is important that the libration angles stay within acceptable limits to ensure tether stability. Deflection-limiting control is needed when the deflection results in libration angles higher than these limits [25, 19, 20, 21]. This deflection is a consequence of the amount of current applied to the tether; therefore, to reduce deflection, the steady-state current must be reduced. This can be accomplished by either reducing the maximum possible current, or by adjusting the command shapers. Adjusting the shapers is an attractive solution because the maximum current can still be used in short bursts without exceeding the maximum desired deflection.

Deflection-limiting command shapers are designed using a modified set of constraint equations.[1] Traditionally, input shaper amplitudes are required to sum to unity to ensure

[1]The deflection-limiting command shaper presented here was developed by Michael Robertson, Ph.D.

that the unshaped and shaped commands have the same setpoint. However, when this setpoint leads to excess deflection, then the impulse magnitude requirement must be reduced. Figure 41 shows the general form of the deflection-limiting shaper proposed here [19, 20, 21]. The first and second impulses have unity magnitude. When these are convolved with a step in current of magnitude I_{max}, the result is a pulse in current of magnitude I_{max} and duration t_2. If the magnitude of A_3 is less than one, then the result is a steady-state current with magnitude $A_3 I_{max} < I_{max}$, resulting in reduced deflection. This process is illustrated in Figure 42.

In order to achieve zero residual vibration, both (2a) and (2b) must be zero. Therefore, the deflection-limiting shaper shown in Figure 41 must satisfy:

$$1 - \cos(\omega t_2) + A_3 \cos(\omega t_3) = 0 \tag{28}$$

$$-\sin(\omega t_2) + A_3 \sin(\omega t_3) = 0 \tag{29}$$

If A_3 can be determined for a desired deflection limit, then (28) and (29) can be solved for t_2 and t_3. Isolating the first cosine term in (28) and squaring the equation yields:

$$\cos^2(\omega t_2) = 1 + 2A_3 \cos(\omega t_3) + A_3^2 \cos^2(\omega t_3) \tag{30}$$

Similarly, (29) yields:

$$\sin^2(\omega t_2) = A_3^2 \sin^2(\omega t_3) \tag{31}$$

Summing (30) and (31) allows us to solve for t_3 [19, 20, 21]:

$$t_3 = \frac{1}{\omega} \arccos\left(-\frac{A_3}{2}\right) \tag{32}$$

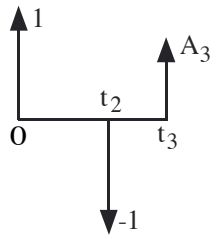

Figure 41: Deflection-limiting command shaper

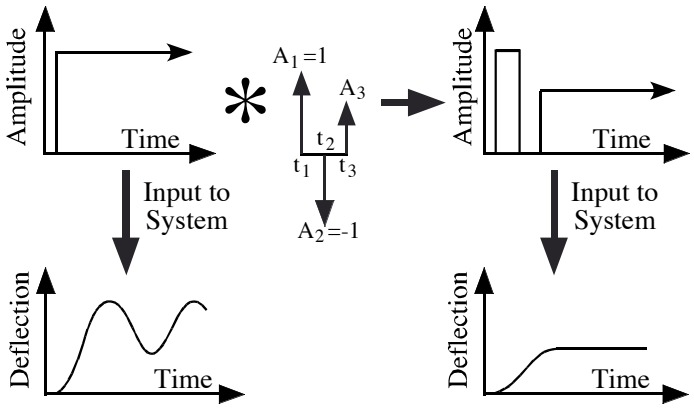

Figure 42: Deflection-limiting command shaping process

This can then be substituted into (28) to find:

$$t_2 = \frac{1}{\omega} \arccos\left(1 - \frac{A_3^2}{2}\right) \tag{33}$$

In order to determine the appropriate value of A_3, a relationship between the applied current and tether deflection must be established. Figure 43 shows the input-shaped response of the tether midpoint deflection as a function of the applied maximum current. The results indicate that a linear relationship between the maximum current and deflection is an adequate assumption. Therefore, the solution proposed here uses a deflection-limiting command shaper designed for the libration mode, while a robust EI shaper is used to suppress the dominant string mode. The amplitude of the third impulse, A_3, can now be determined by the desired deflection reduction relative to the case with full current. For example, if the

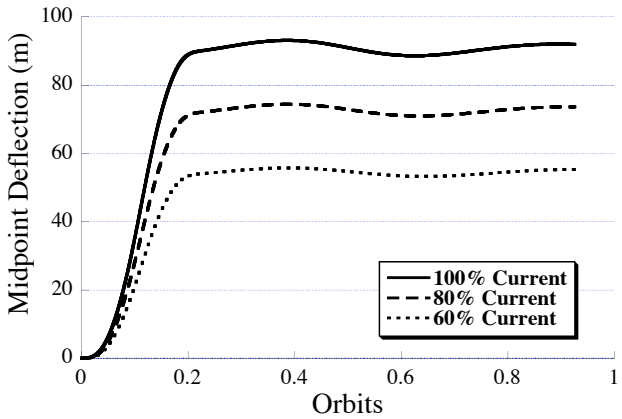

Figure 43: Deflection-limiting command shaping for current input

deflection from a traditional shaper is 100 meters, and the deflection should not exceed 80 meters, then a 0.80 deflection-limiting shaper (A_3=0.8) is derived using (32) and (33). This shaper is then convolved with an EI shaper to reduce the string vibration. This process is illustrated in Figure 44.

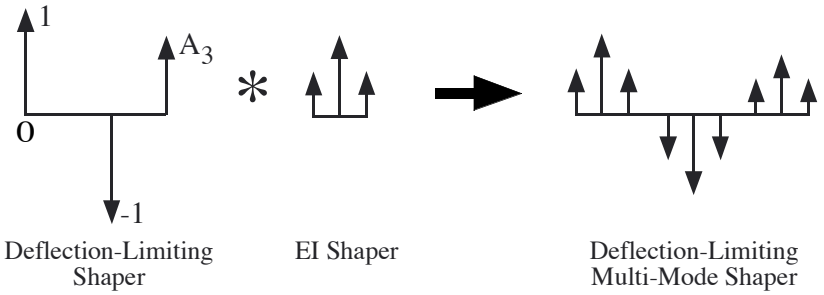

Figure 44: Combined deflection-limiting and robust input shaper

3.2 Input Shaping Robustness Analysis

3.2.1 Traditional Input Shaping

Another issue that needs to be investigated is the robustness of input shaping to variations in system parameters. We will start by demonstrating the robustness of the non-deflection-limiting shapers introduced first. Figure 45 shows the amplitude of the peak-to-peak residual vibration of the tether midpoint for a variation in subsatellite mass from 400 to 600 kilograms when the input shaper was designed for a 500 kilogram subsatellite mass. As can

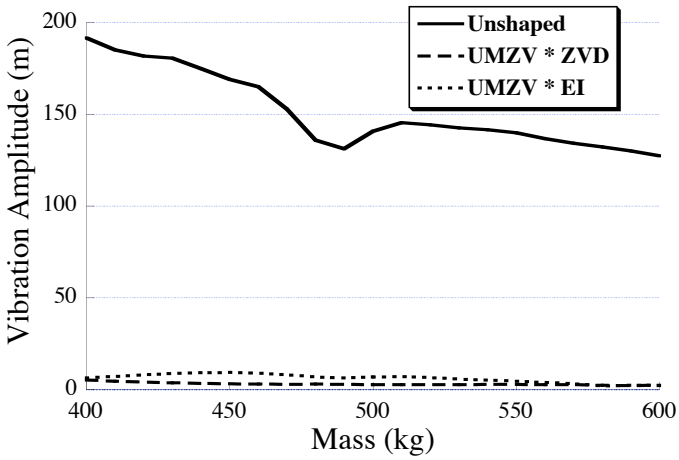

Figure 45: Sensitivity of shaping to subsatellite mass

be seen, the implementation of input shaping drastically reduces the amount of vibration for the entire range of subsatellite masses. When the command is not shaped, the string vibration and the libration combine to give the overall oscillation amplitude, such as that shown in Figure 36. In some cases, the oscillation peaks of the individual modes combine, and in other cases, they destructively interfere. This destructive interference causes the slight dip in the unshaped vibration amplitude that occurs near a subsatellite mass of 480 kg.

Another important parameter that affects the dynamic response is the orbital altitude. Because the main goal of electrodynamic reboost is to change orbital altitude, this parameter will naturally vary throughout the life of the system. Figure 46 shows the tether midpoint vibration amplitude for a variation in orbital altitude from 190 km to 210 km. Once again, the shaped vibration is negligible when compared to the unshaped vibration across the entire range shown. Furthermore, large changes in orbital altitude do not significantly affect the vibration amplitude.

3.2.2 Deflection-Limiting Input Shaping

Robustness studies were also completed to determine the effect of parameter variations on the system performance when deflection-limiting input shaping is used. Because we are also

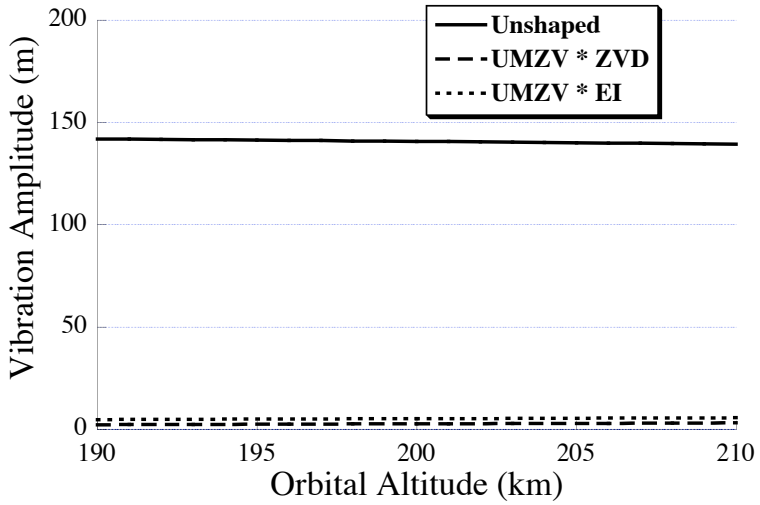

Figure 46: Sensitivity of shaping to orbital altitude

concerned with the maximum tether deflection, it is plotted along with residual vibration data in this section. Figure 47 shows the residual vibration and maximum deflection of the tether midpoint as the subsatellite mass varies from the nominal design value of 500 kg. The new command shaping method works as expected to lower the maximum transient deflection. In all cases, the maximum deflection decreases as the subsatellite mass increases. Figure 48 shows the effect that variations in tether stiffness (as measured by EA) have on the tether response. Because the tether stiffness mainly affects the longitudinal wave properties and not the transverse dynamics, the vibration amplitude is basically unaffected by changes in tether stiffness. A more important parameter for transverse dynamics is the tether density. Figure 49 shows the shaper performance when the tether density per unit length varies from the baseline value of 1 kg/km. The results indicate that the command shaping technique is very robust to density changes. The results shown in Figures 47 – 49 indicate that the proposed command shaping technique has good robustness to parameter variations.

3.3 Conclusions

This chapter has established that input shaping is an effective method of reducing transverse vibration in electrodynamic space tethers. Input shaping is able to reduce both pendulum-like librations and string vibrations. It is also possible to use input shaping to decrease the maximum tether deflection. This reduces the tether libration angle, which is important for tether stability.

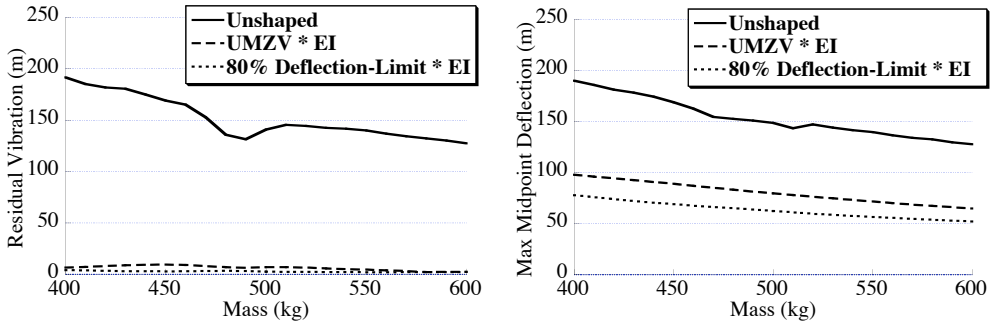

(a) Residual vibration (b) Maximum transient deflection

Figure 47: Shaper performance with variations in endpoint mass

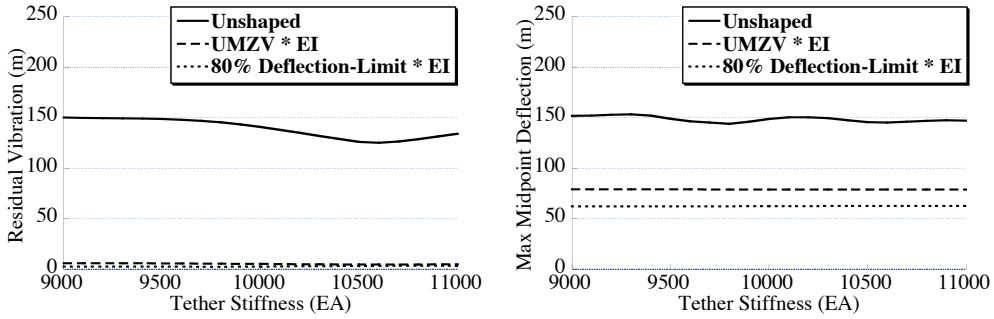

(a) Residual vibration (b) Maximum transient deflection

Figure 48: Shaper performance with variations in tether stiffness

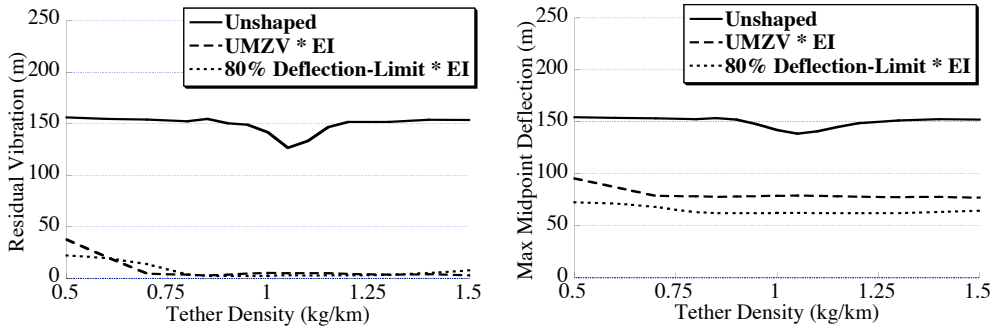

(a) Residual vibration (b) Maximum transient deflection

Figure 49: Shaper performance with variations in tether density

The application of input shaping to electrodynamic tethers represents a major advancement to current tether technology. Without sophisticated vibration control, electrodynamic orbit boosting is not possible. This control is difficult to achieve through any type of feedback control design because sensing of the tether dynamics is incredibly difficult to obtain. Input shaping offers an easily implementable tool to provide the vibration reduction necessary to make electrodynamic tether boosting missions possible. Input shaping is also robust to modeling errors. In the next chapter, this work will be extended to the case of orbit boosting with electrodynamic tethers.

CHAPTER IV

INPUT SHAPED ORBIT BOOSTING OF ELECTRODYNAMIC TETHERS

In the previous chapter, input shaping was used to greatly reduce unwanted oscillatory dynamics in constant orbit tethers. These same techniques can be utilized for orbit boosting maneuvers. The model used in this section was developed by Arun Banerjee at Lockheed Martin Advanced Technology Center and is described in detail in Reference [2]. The concept is the same as the model used in Chapter 3 and shown in Figure 35. However, the model used in this chapter does include the effects of changing orbit. It also uses a two-part tether, with electrodynamic forces present on the upper half of the tether and aerodynamic drag forces present on the lower half. The model output is expanded over the constant-orbit model by generating tether libration angles, midpoint deflection, and orbital altitude. The tether midpoint deflection is measured as the perpendicular distance from the line of sight from one end of the tether to the other. The equations of motion for this model were derived in AUTOLEV. The AUTOLEV code used to generate the simulation code is given in Appendix B. The shortcomings of this orbit-boosting model are:

- The Earth's magnetic field is modeled as a tilted dipole, ignoring certain harmonic terms.
- Earth oblateness effects are not modeled. These effects will add to the out-of-plane tether libration.
- Current collection dynamics, including variations in ionospheric electron density, are ignored.
- The model uses only five node masses to model the tether. Increasing the number of these masses may change the string vibration behavior of the tether.

4.1 Simulation and Input Shaping Results

4.1.1 Frequency Content Analysis

Table 2 summarizes the simulation parameters used in this chapter. These parameters are labeled on the sketch of the model shown in Figure 50. To find the frequency content of the tether response, a 1.5 A current pulse was sent through the tether for 2320 seconds, and FFT's were performed on each of the simulation output measures. Because this simulation also captures orbital behavior, including orbital altitude variations, some of the frequencies of interest are considerably lower than in the previous chapter.

The first output measure we examine in detail is the orbital altitude. When given a pulse thrust, a satellite in a circular orbit will move to an elliptical one. This eccentricity shows up as oscillations in the orbital altitude. The oscillation amplitude is determined by

Table 2: Simulation parameters.

Simulation Parameter	Nominal Value
Tether Length, L	20 km
Tether Density, ρ	1 kg/km
Equivalent Spring Constant, K	8 kN/km
Mother Satellite Mass, m_m	300 kg
Daughter Satellite Mass, m_d	5 kg
Initial Orbital Altitude, H	500 km
Orbital Inclination, i	50°

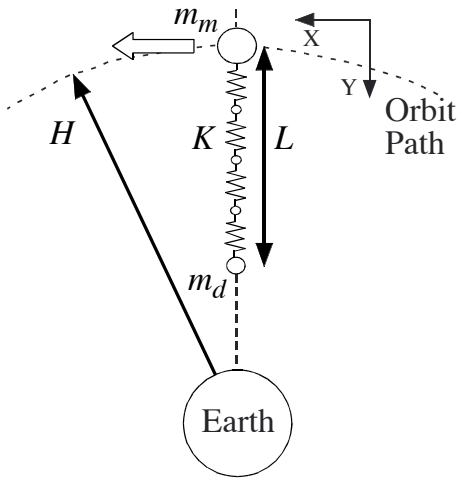

Figure 50: Schematic of model with simulation parameters

the apogee and perigee of the orbit, and the frequency is the orbital frequency. For the initial altitude chosen here, the orbital period is approximately 5660 seconds.

Next, tether libration is reviewed. In-plane tether libration (θ) has two relevant frequency components with periods of 3279 and 1282 seconds, while out-of-plane libration (ϕ) has one main component at 2844 seconds. The in-plane libration frequency agrees with the 10-node-mass model of the previous chapter to within 7%.

Figure 51 shows the frequency content of the tether midpoint deflection. This shows much higher frequencies of vibration than that of orbital altitude variations and libration angles. It also exhibits more than one significant mode. The modes considered in this investigation correspond to the three largest spikes seen in Figure 51 and have periods of 641, 617, and 537 seconds. These frequencies are different than those seen in Chapter 3. The constant-orbit model utilized 10 node masses and was given a step reference input. The orbit-boosting model used here contains only 5 node masses and is given a pulse current input. Also, the midpoint deflection measure used here is different than that used previously. This model uses deflection from the line of sight, while the constant-orbit model used deflection measured from the line connecting the constant-orbit mother satellite with the center of the Earth. These differences explain the differences in frequency content.

4.1.2 Single-Mode Shaping

In order to determine how effective input shaping is at reducing oscillations in each of the three dynamic effects being studied, namely libration, string vibration, and orbital eccentricity, separate input shapers designed for each type of vibration were developed

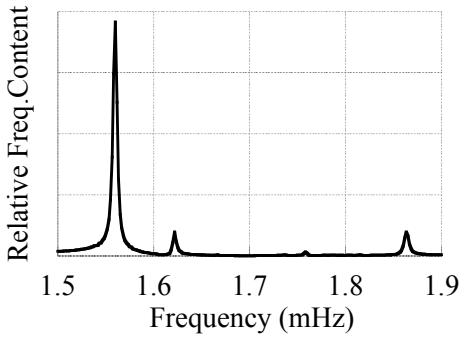

Figure 51: Midpoint deflection frequency content.

independently. A variety of shapers were tested for each type of vibration, including ZV, UMZV, ZVD, and EI.

The pulse response of the system's orbital altitude exhibits oscillatory behavior evident in the unshaped response of Figure 52. These oscillations in orbital altitude represent the transition of the tether from a circular to an elliptical orbit. A common method of raising a satellite from one circular orbit to another is to apply a pulse to raise the apogee and then apply a second pulse after one-half revolution to circularize the orbit.

If this method is examined from the standpoint of input shaping, it is equivalent to a single pulse convolved with a ZV shaper tuned to the orbital frequency. Thus, if the orbit eccentricity is treated as an oscillation to be minimized, a variety of input shapers should be readily applicable to orbit circularization. This is confirmed by the success of input shaping to eliminate oscillations in orbital altitude as evidenced by the shaped responses in Figure 53. These oscillations can be further reduced by using a more robust shaper such as the ZVD shaper. The ZVD shaper, however, will take a full cycle to complete. Since the cycle is an entire orbit, this time penalty may be too great for the slight decrease in eccentricity. Because orbital oscillations have such a long period, it is desirable for any input shaper used to be fast. Negative shapers such as the UMZV are faster than positive shapers, but they also have the added danger of high-mode excitation. If the pulse duration is less than one third of an orbital period, UMZV shapers will also produce negative thrust, wasting fuel. As seen in Figure 53, the UMZV shaper does exhibit a faster rise time, but the lack of

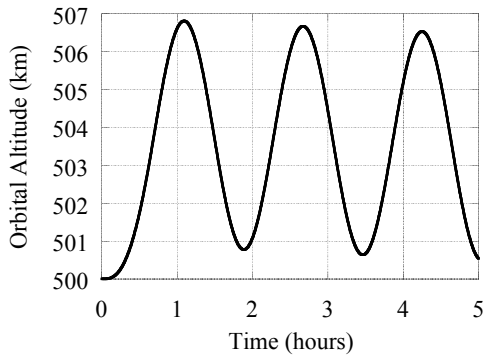

Figure 52: Orbital altitude response to unshaped current pulse

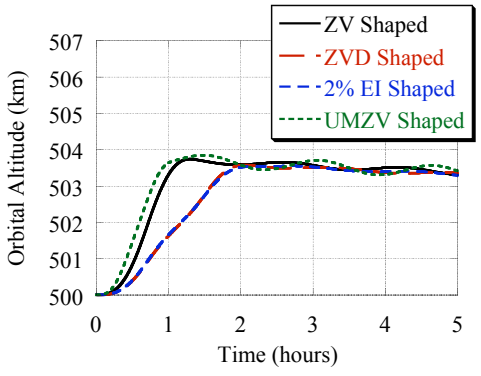

Figure 53: Orbital altitude response to shaped current pulses

significant damping and extreme flexibility of tethers in space may preclude the application of negative shapers due to their tendency to excite high modes.

Figure 54 shows the in-plane tether libration response when driven with a current pulse. The unshaped current pulse induces large amounts of tether libration, approximately 8° in each direction. Figure 55 shows that input shaping successfully reduces the amount of libration to around 2°, but cannot completely eliminate the libration. This is due to the effect of the elliptical orbit on the gravity gradient forces acting on the tether. In an elliptical orbit, the orbit normal is not in a constant orientation; rather, it changes as the satellite moves through its orbit. This causes increased libration, as noted by Peláez and Andres [18].

Figure 56 shows the corresponding unshaped out-of-plane libration. This exhibits similar behavior to the in-plane libration, but it appears to have less complicated frequency content than the in-plane libration. Figure 57, however, shows that input shaping is much less effective at reducing librations normal to the orbital plane. This is due to the interaction between the Earth's magnetic field and the line of the tether which determines the direction of the electrodynamic (ED) force. This interaction depends on the inclination of the tether orbit. As the inclination varies from zero degrees, the ED forces start to have components out of the orbital plane. This effect is responsible for the out-of-plane libration seen here. Because there is less actuation out of the plane, however, input shaping is less effective.

Figure 58 shows the magnitude of the tether midpoint deflection for an unshaped current

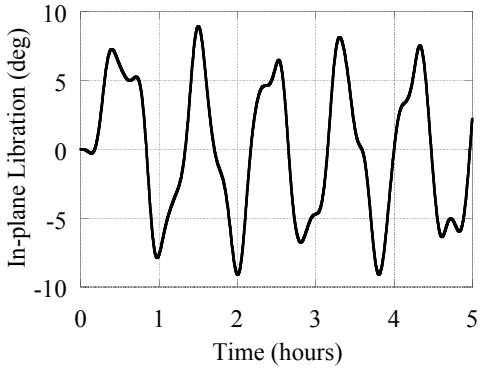

Figure 54: In-plane tether libration response to unshaped current pulse

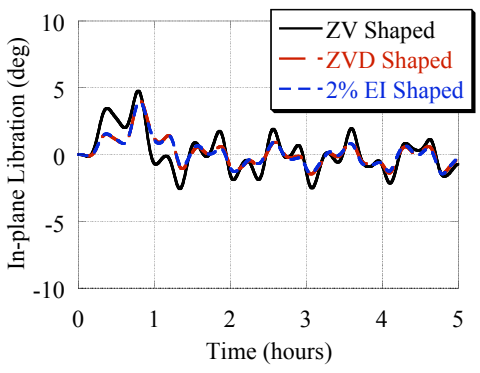

Figure 55: In-plane tether libration response to shaped current pulses

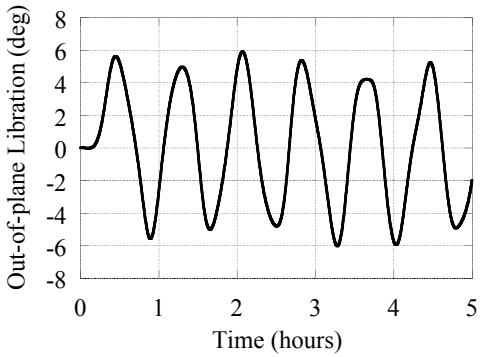

Figure 56: Out-of-plane tether libration response to unshaped current pulse

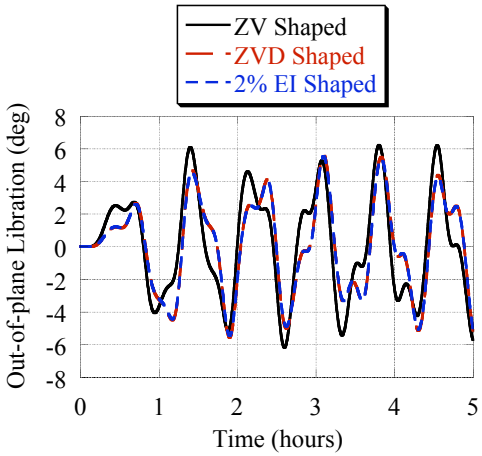

Figure 57: Out-of-plane tether libration response to shaped current pulses

pulse. When a single ZV shaper is applied to the current, these higher frequency oscillations are reduced over 50%, from 203 m to 93 m, as seen in Figure 59. Figure 59 shows only the first half of the tether response for ease of presentation. Because these are higher frequency oscillations, however, shaper duration is much less of an issue when compared to orbital altitude shapers. With this in mind, more robust shapers can be applied to the midpoint deflection if necessary. Applying ZVD shaping for the dominant string mode further reduces vibration, but the response clearly shows multiple modes of vibration are present. Further improvement requires the use of multi-mode shaping.

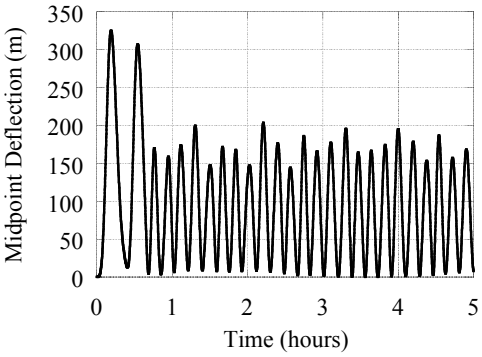

Figure 58: Tether midpoint deflection response to unshaped current pulse

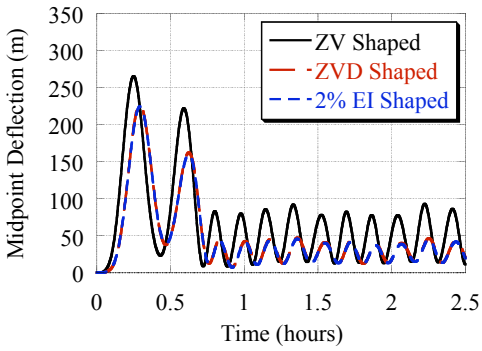

Figure 59: Tether midpoint deflection response to shaped current pulses

4.1.3 Multi-Mode Shaping

Now that input shaping has proven effective for reducing oscillations in orbital altitude, in-plane tether libration, and tether midpoint string vibration, it is time to design an input shaping controller to achieve vibration reduction in all problem areas. The first multi-mode shaper presented here is a convolved shaper that targets these effects. Because of its relatively fast response, a ZV shaper is used to reduce orbital altitude oscillations. A UMZV shaper could be used for this mode, but the dangers of high-mode excitation outweigh the small decrease in system rise time. Three 2% EI shapers are chosen for the other modes of vibration. One is tuned to the dominant in-plane libration frequency, and two are tuned to two of the string frequencies. Two percent EI shapers offer the increased robustness helpful in dealing with these highly nonlinear effects. Figure 60 shows the tether response to a 1.5 A, 2320 s current pulse shaped by this multi-mode shaper. The shaper performs very well at reducing residual oscillation in all of the performance measures. The only problems

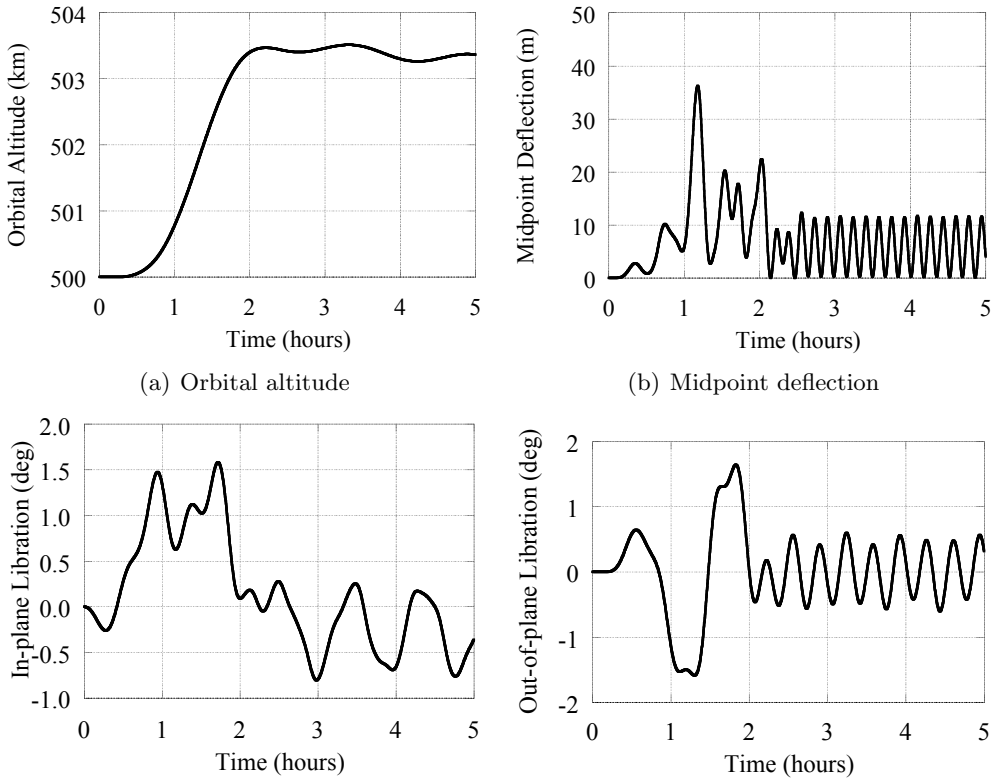

(a) Orbital altitude

(b) Midpoint deflection

(c) In-plane libration

(d) Out-of-plane libration

Figure 60: Tether response to convolved four-mode shaped pulse

with this shaper are that it has quite a long rise time, and it is very complex, containing 54 impulses.

To try to increase the speed and decrease the complexity of the input shaper, the maximum current amplitude is decreased to 1 A while the unshaped current pulse is lengthened to 3480 s to achieve the same energy input to the system. In addition to the less aggressive input, the in-plane libration is left unshaped. This results in a three-mode convolved shaper addressing the orbital altitude and midpoint deflection. The length of the input is shorter than the previous shaper, and the shaper is reduced from 54 impulses to 18. This reduction in complexity is desirable as it makes the current input easier to implement. The tether response to this shaped input is shown in Figure 61. The transient dynamics are more pronounced for this less complex shaper, but it is just as effective for vibration reduction. The only notable differences are the further reduction in midpoint deflection seen when comparing Figure 61(b) to 60(b) and the faster rise time of the three-mode shaper seen

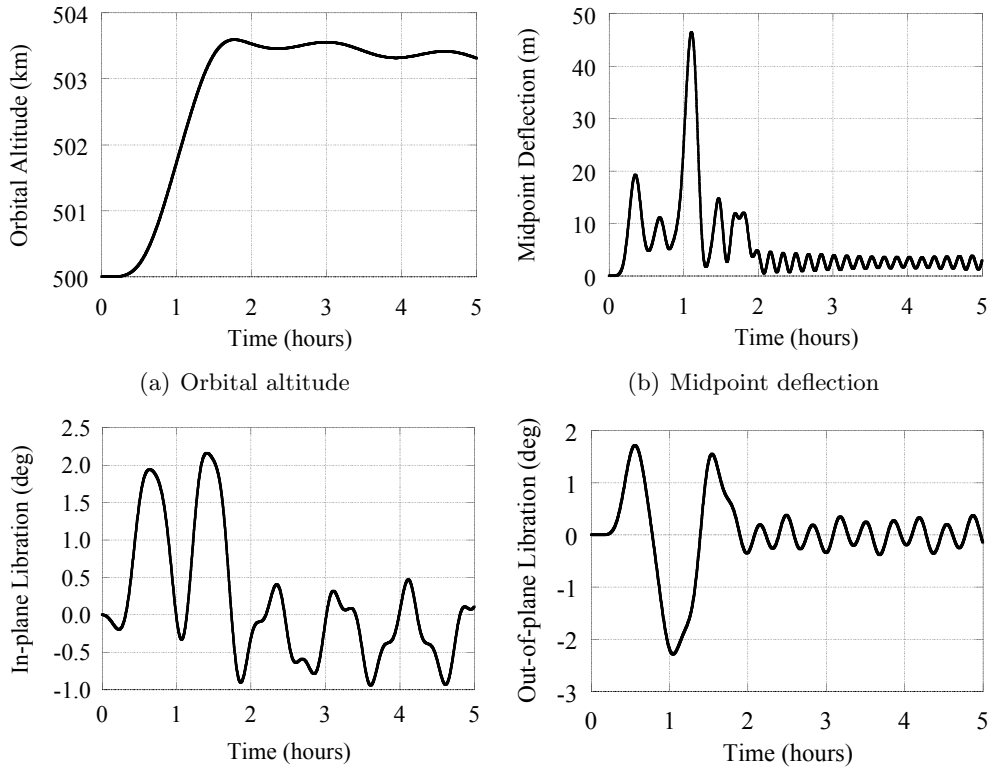

(a) Orbital altitude

(b) Midpoint deflection

(c) In-plane libration

(d) Out-of-plane libration

Figure 61: Tether response to convolved three-mode shaped pulse

when comparing Figure 61(a) to 60(a).

Another way to produce shapers for multiple modes of vibration is to solve the vibration and robustness constraints for each frequency simultaneously. This will often result in a faster, slightly less robust input shaper [26]. Based on the success of the low-current three-mode shaper, similar constraints are used in the simultaneous shaper design. The orbital frequency was subjected to ZV constraints while string vibration frequencies were subjected to ZVD constraints. The resulting shaper contains only 6 impulses, making it much easier to implement. The shaper amplitudes and times are given by:

$$\begin{bmatrix} A_i \\ t_i \end{bmatrix} = \begin{bmatrix} 0.093 & 0.242 & 0.165 & 0.165 & 0.242 & 0.093 \\ 0 & 323 & 647 & 2923 & 3247 & 3570 \end{bmatrix}, \qquad i = 1, \ldots, 6 \tag{34}$$

The simultaneous shaper is also about 6% faster than the previous convolved shaper. Figure 62 shows the tether response to the simultaneous shaper. The responses are very similar to that of the three-mode convolved shaper. Because the convolved shaper will have more

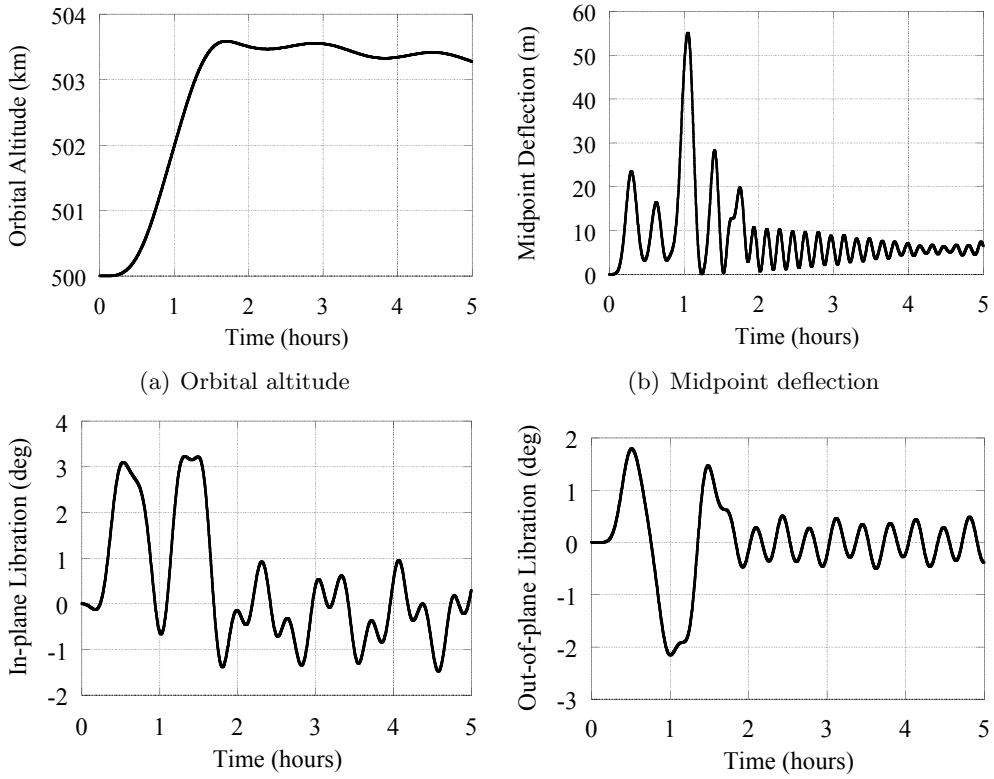

(a) Orbital altitude

(b) Midpoint deflection

(c) In-plane libration

(d) Out-of-plane libration

Figure 62: Tether response to simultaneous three-mode shaped pulse

robustness to errors in the higher frequencies than the simultaneous shaper, it is used for the remainder of this study.

4.2 Input Shaping Robustness Analysis

Now that a suitable input shaping scheme has been developed, it must be analyzed for sensitivity to modeling errors. The input shapers were designed for nominal modeling frequencies and damping ratios. When the system parameters deviate from their assumed values, these frequencies will change, possibly leading to degraded performance. For this section, the input shaper being tested is the convolved three-mode shaper with system response shown in Figure 61. Figure 63 shows the residual oscillation for each of the output measures when the initial orbital altitude is varied from 400 km to 600 km. Input shaping successfully reduces residual oscillation in every dynamic effect for the entire range of initial

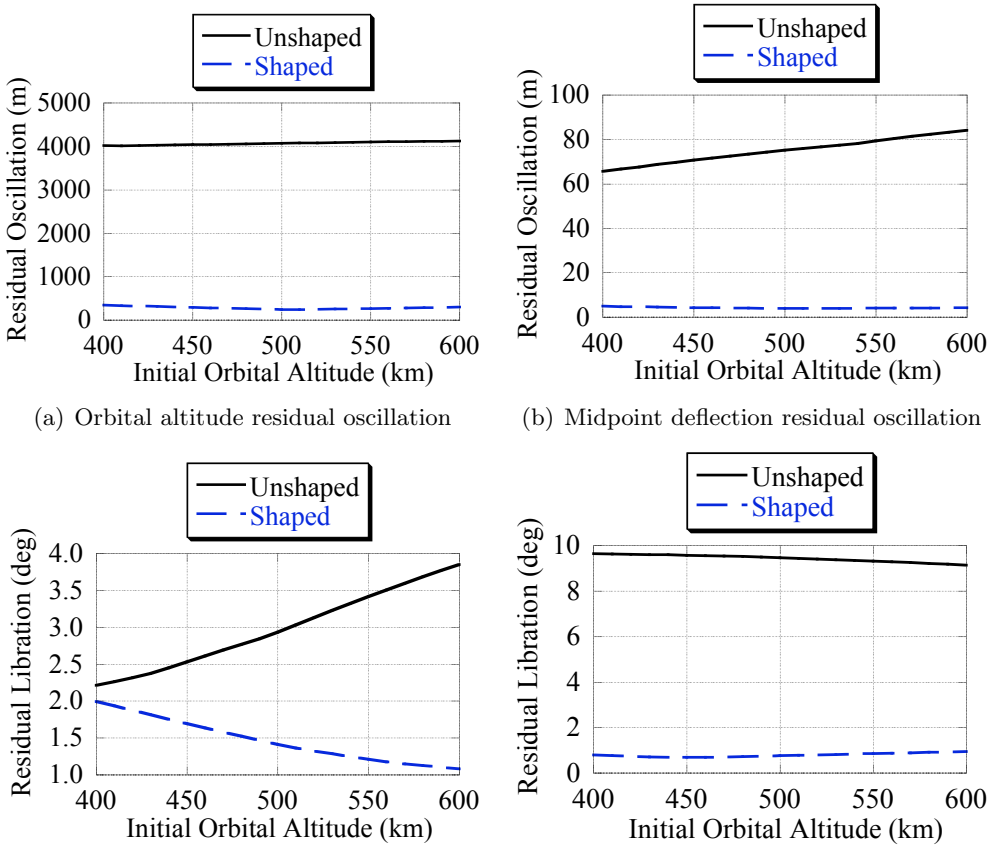

(a) Orbital altitude residual oscillation

(b) Midpoint deflection residual oscillation

(c) Residual in-plane libration

(d) Residual out-of-plane libration

Figure 63: Sensitivity to changes in initial orbital altitude

altitudes. The shaper shows the most sensitivity to in-plane libration angles, as these were not specifically addressed in the shaper design. It is interesting to note, though, that for increasing orbital altitude, the shaped tether libration decreases. As the orbital altitude increases, the magnitudes of the electrodynamic forces decrease. The forces generated at 600 km are approximately 10% lower than those generated at 400 km. This could explain the decrease in libration angle, as lowering the current (and hence the force) was already shown to drastically reduce the in-plane tether libration. Figure 64 shows the shaper's sensitivity to variations in tether density. Even with a variation in density of ± 30%, the input shaper is able to reduce residual oscillations to a fraction of their unshaped values.

More interesting phenomena occur when the orbital inclination is varied from 0 to 90 degrees. Figure 65 shows residual oscillation for varying orbital inclination. Changing the inclination drastically changes the orientation of the magnetic field lines. At low inclinations,

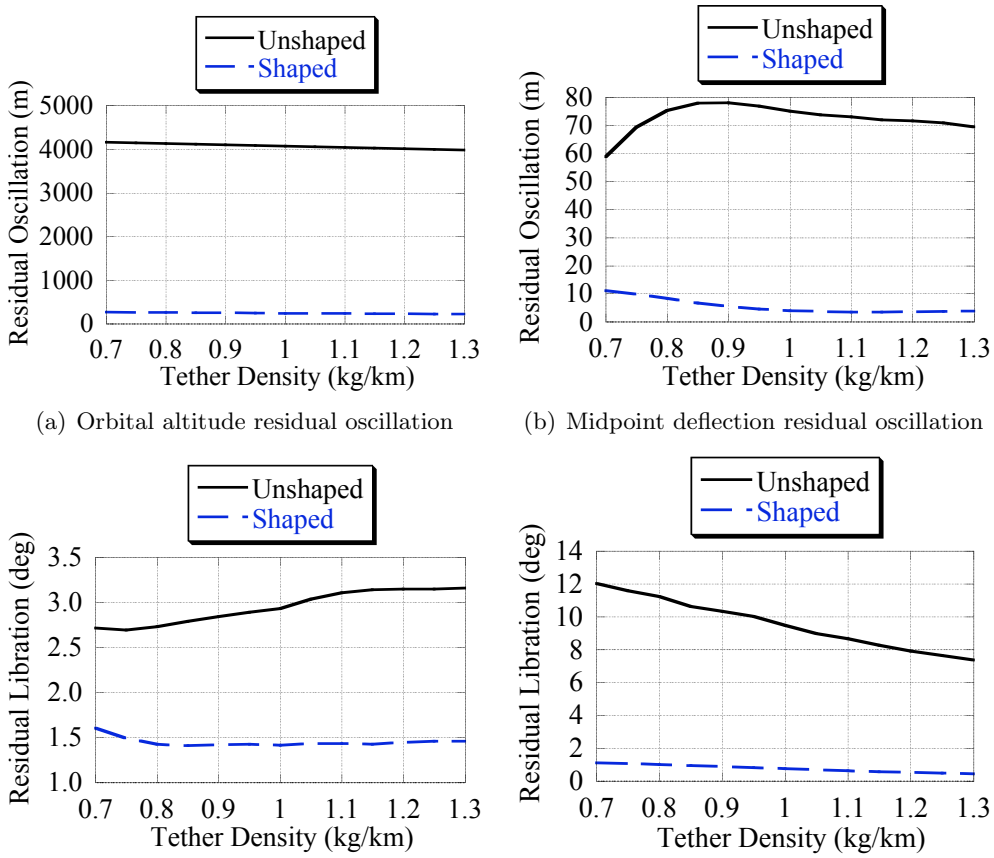

(a) Orbital altitude residual oscillation

(b) Midpoint deflection residual oscillation

(c) Residual in-plane libration

(d) Residual out-of-plane libration

Figure 64: Sensitivity to changes in tether density

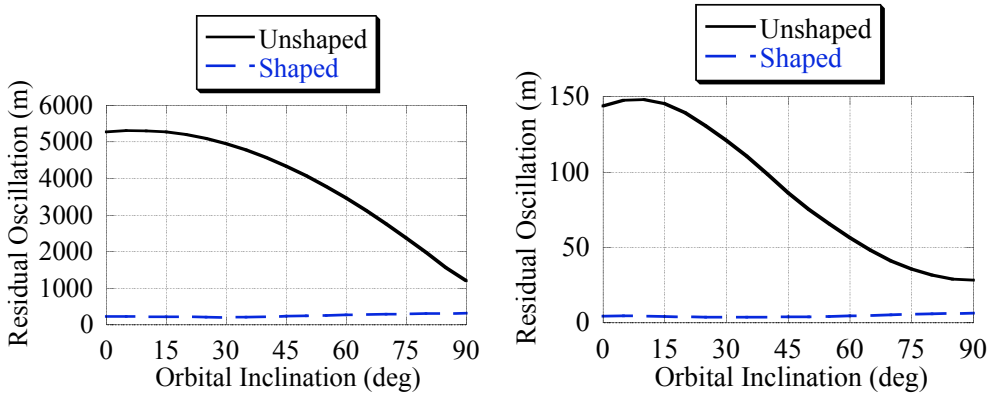

(a) Orbital altitude residual oscillation

(b) Midpoint deflection residual oscillation

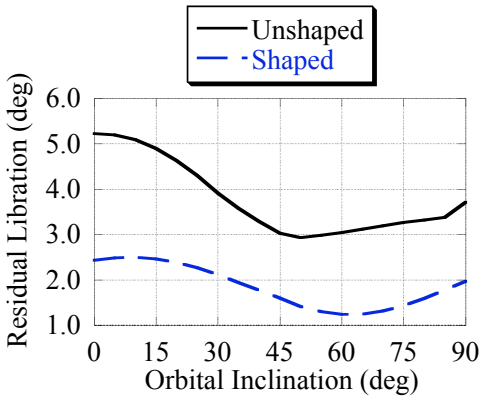

(c) Residual in-plane libration

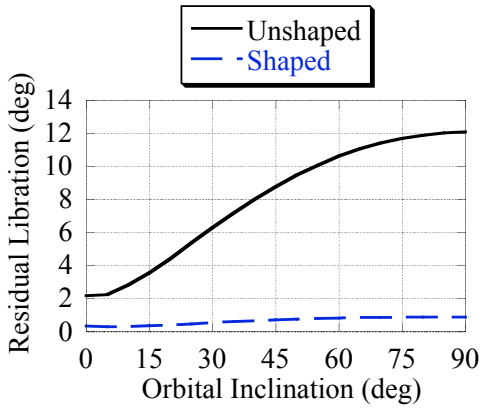

(d) Residual out-of-plane libration

Figure 65: Sensitivity to changes in orbital inclination

the magnetic field lines are nearly perpendicular to the tether, allowing for large magnitude forces in the orbital plane. As the inclination increases, the tether starts to become aligned with the magnetic field lines, reducing the potential for orbit boost and magnifying the out-of-plane librations. This explains the large variations in residual altitude oscillations present in the unshaped tether response: the apogee is being boosted more for more equatorial orbits. This variation is not present in the shaped responses, however. The input shaper still circularizes the orbit, regardless of the inclination. The final orbital altitude of the shaped responses will be different for each inclination, however. This is illustrated in Figure 66. At 0° inclination, the tether is in the best orientation to provide forces in the direction of orbit boosting, leading to the greatest increase in altitude. At a polar orbit ($i = 90°$), there is virtually no force in the direction necessary for orbit boost, and, consequently, very little boosting occurs.

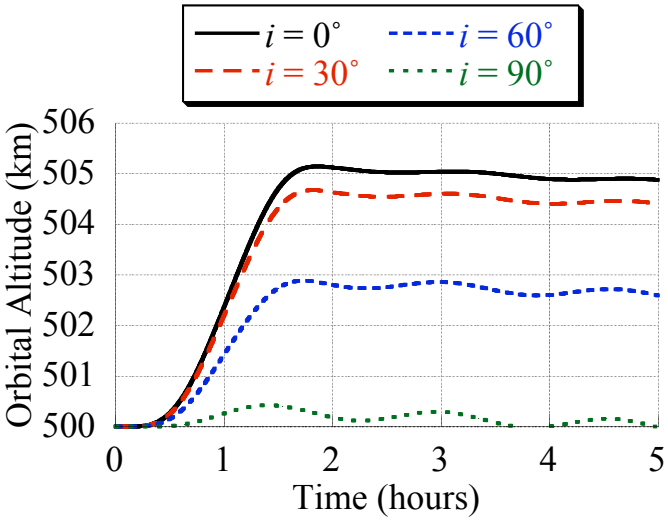

Figure 66: Orbital altitude response to shaped current pulse for varying inclination

4.3 Conclusions

An input shaping controller was developed for reducing command-induced vibration in electrodynamic space tethers. It is able to improve oscillation behavior in all of the effects present in the tether dynamics studied thus far, including libration, string vibration, and orbital eccentricity. Input shapers designed for multiple modes of vibration greatly reduced unwanted oscillatory dynamics and were demonstrated to be very robust to modeling errors. This input shaping controller makes electrodynamic orbit boosting possible, presenting a viable, cost-effective alternative to chemical propulsion.

The application of input shaping to orbit circularization presents a new way of approaching this problem. A variety of input shapers are readily applicable to the boosting of circular orbits, as illustrated by Figure 53. Using these shapers with a simple pulse thrust offers a very simple alternative to complex, continuous time solutions.

CHAPTER V

CONCLUSIONS AND FUTURE WORK

5.1 Conclusions

Every mechanical system will exhibit some type of oscillatory behavior. This is often a major problem with lightweight, flexible machines. For systems with cable elements, this problem is often complicated by the presence of significant nonlinear dynamics. Reducing crane payload oscillations allows crane operators to have much higher throughputs on the machines. It also makes automation or remote operation possible for cranes that work in inhospitable environments. Input shaping can provide this reduction in payload oscillation in an easily implementable package.

A novel input shaping algorithm based on nonlinear directional effects improves the performance of ZV shaping in tower crane slewing motions. This radial assist shaper requires only minimal knowledge of the system parameters. It does not delay the system any more than traditional ZV shaping and also provides a significant performance increase. This advances the current state of input shaping technology on nonlinear systems by improving vibration reduction and offering a new perspective on the problem of rotational motion. The directional design algorithm represents a new approach to command shaper design for tower cranes and could also be extended to more robust input shapers such as ZVD and EI. The increased performance of the radial assist slewing shaper was verified by experimental results, proving its effectiveness.

The application of input shaping to electrodynamic space tethers represents a major advancement to current tether technology. Input shaping offers a highly effective, easily implementable solution to the problem of large-scale tether oscillations. Without an effective method for controlling vibrations, electrodynamic tethers will not be a viable option for spacecraft propulsion. Input shaping is able to reduce oscillation in a number of the dynamic effects seen in space tethers and, thus, provides the vibration control necessary to make

electrodynamic orbit boosting feasible.

Viewing circular orbit boosting from the perspective of an input shaping problem greatly simplifies the design of the necessary thrust profiles. A variety of input shapers are readily applicable to the boosting of circular orbits, as demonstrated in Chapter 4. Using these shapers with a simple pulse thrust offers a very simple alternative to complex, continuous time solutions.

5.2 Future Work

The current work on slewing shapers for tower cranes can be extended to the case of robust three impulse input shapers such as ZVD and EI. Constraining three impulses to be in the same direction may produce an indeterminate system, with the direction being an under-constrained variable. Also, more experimental testing could determine the importance of radial velocity tracking error in the implementation of this input shaper. Improved velocity tracking requires either hardware capable of high-precision tracking or velocity profiles that are easy to track. Because the radial velocity depends directly on the steady-state slewing velocity, increasing the velocity of the slew makes the radial velocity profile easier to track, but also presents the possibility of causing structural damage to the crane. These structural issues impose a limit on the maximum slewing velocity, limiting the radial velocity as well. The desired radial velocity also directly depends on the radial position of the trolley at the start of the slew. Thus, increasing the starting radius will provide more trackable radial velocity profiles. Centripetal effects also influence the payload response more at larger radii. High-speed slews at large radii may magnify the performance improvements of the radial assist shaper over traditional input shapers.

Refinement of the electrodynamic tether orbit boosting model could also further demonstrate the effectiveness of input shaping in a very complex nonlinear system. The number of discrete masses used in the simulation can be increased to ensure the fidelity of the model. The effects of Earth oblateness can also be included to determine their influence on out-of-plane tether librations in inclined orbits. This may be a problem that input shaped current cannot alleviate, due to the orientation of the electrodynamic forces. Additional actuation

may be needed to control the out-of-plane librations. The area of space tether research is one with a bright future. Many applications exist where tethers offer a very attractive solution. However, many issues exist with the control of all stages of their operation, and, as such, there will continue to be research on space tether dynamics for years to come.

APPENDIX A

EQUATIONS OF MOTION FOR CONSTANT-ORBIT TETHER MODEL IMPLEMENTED IN MATLAB

```
function ydot=eqns(t,y,flag,n,mu,m,Ls,EA,c_eq,t_final,e,p_orbit,shap)
%%%%%%%%%%%%%%%%%%%%%%%%%%%%%%%%%%%%%%%%%%%%%%%%%%%%%%%%%%%%%%%%%%%%%%%%%%%%
% Kinematic Equations for Kane's Equations
% u1 = y(3*n+3+1) ... etc

f=y(6*n+1);    % true anomaly
% Keplerian orbit parameters
k = 1+e*cos(f);
R = p_orbit/k;
Rdot = sqrt(mu/p_orbit)*e*sin(f);
omega=sqrt(mu/p_orbit^3)*k^2;

% Magnetic field stuff
M_mag = (7.8123*10^30)/(100^3)/(10^9);
perigee = 0;
inc = 45*pi/180;
Bx = -2*M_mag/R^3*sin(perigee+f)*sin(inc);
By = M_mag/R^3*cos(perigee+f)*sin(inc);
Bz = M_mag/R^3*cos(inc);

%%%%%%%%%%%%%%%%%%%%%%%%%%%%%%%%%%%%%%%%%%%%%%%%%%%%%%%%%%%%%%%%%%%%%%%%%%%%
%%Set the current profiles
```

```
maxcurrent=1;

% use the input shaper to determine the desired current level
% the shaper is in shap[n,2]= [times amplitudes]
% shap=[0 .25;90 .5;180 .25];  %ZVD shaper

flag=0;
if (t<=shap(2,1))
   current=shap(1,2)*maxcurrent;
   flag=1;
end

for i=2:length(shap)-1
   if ((t>shap(i,1)) & (t<=shap(i+1,1))),
      current=sum(shap(1:i,2))*maxcurrent;
      flag=1;
   end
end

if (flag ~=1)
   current=sum(shap(:,2))*maxcurrent;
end

%%%%%%%%%%%%%%%%%%%%%%%%%%%%%%%%%%%%%%%%%%%%%%%%%%%%%%%%%%%%%%%%%%%%%%%%%%%%
% Variables describing tether tip

rk = y(6*n+2);
thetak = y(6*n+3);
```

```
phik = y(6*n+4);


for j=1:n
   u(3*(j-1)+1)=y(3*n+3*(j-1)+1);
   u(3*(j-1)+2)=y(3*n+3*(j-1)+2);
   u(3*(j-1)+3)=y(3*n+3*(j-1)+3);
end


for j=1:n
   if j==n   %boundary condition(subsatellite)
      ydot(3*(n-1)+1)=u(3*(n-1)+1)+omega*y(3*(n-1)+2)-Rdot;
      ydot(3*(n-1)+2)=u(3*(n-1)+2)-omega*(R+y(3*(n-1)+1));
      ydot(3*(n-1)+3)=u(3*(n-1)+3);
   else
       ydot(3*(j-1)+1)=u(3*(j-1)+1)-u(3*j+1)+omega*y(3*(j-1)+2);
       ydot(3*(j-1)+2)=u(3*(j-1)+2)-u(3*j+2)-omega*y(3*(j-1)+1);
      ydot(3*(j-1)+3)=u(3*(j-1)+3)-u(3*j+3);
    end
 end

%%%%%%%%%%%%%%%%%%%%%%%%%%%%%%%%%%%%%%%%%%%%%%%%%%%%%%%%%%%%%%%%%%%%%%%%%%%%
% Newtonian Gravity Forces

for j=1:n
   rc(1)=R;
   rc(2)=0;
   rc(3)=0;
   for k=j:n
      rc(1) = rc(1) + y(3*(k-1)+1);
```

```
      rc(2) = rc(2) + y(3*(k-1)+2);
      rc(3) = rc(3) + y(3*(k-1)+3);
   end
   r(j) = sqrt(rc(1)^2+rc(2)^2+rc(3)^2);
   % Calculate gravity forces, Newtonian field
   Fg(3*(j-1)+1) = -mu*m(j)/(r(j)^3)*rc(1);
   Fg(3*(j-1)+2) = -mu*m(j)/(r(j)^3)*rc(2);
   Fg(3*(j-1)+3) = -mu*m(j)/(r(j)^3)*rc(3);
end

%%%%%%%%%%%%%%%%%%%%%%%%%%%%%%%%%%%%%%%%%%%%%%%%%%%%%%%%%%%%%%%%%%%%%%%
% Spring Forces on Tether Lumped Masses
% Pure spring model

for j=1:n
   spring_length(j) = sqrt(y(3*(j-1)+1)^2+y(3*(j-1)+2)^2+y(3*(j-1)+3)^2);
   K_factor(j) = EA/Ls(j)*(1-Ls(j)/spring_length(j));
   D_factor(j) = c_eq*(ydot(3*(j-1)+1)*y(3*(j-1)+1)+
         ydot(3*(j-1)+2)*y(3*(j-1)+2)+ydot(3*(j-1)+3)*y(3*(j-1)+3))/
         spring_length(j)^2;
end

for j=1:n
   % End grapple/payload mass
   if j==1
      Fs(3*(j-1)+1)=-K_factor(1)*y(3*(j-1)+1);
      Fs(3*(j-1)+2)=-K_factor(1)*y(3*(j-1)+2);
      Fs(3*(j-1)+3)=-K_factor(1)*y(3*(j-1)+3);
      Fd(3*(j-1)+1)=-D_factor(1)*y(3*(j-1)+1);
```

```
      Fd(3*(j-1)+2)=-D_factor(1)*y(3*(j-1)+2);
      Fd(3*(j-1)+3)=-D_factor(1)*y(3*(j-1)+3);
   else
      Fs(3*(j-1)+1)=K_factor(j-1)*y(3*(j-2)+1)-K_factor(j)*y(3*(j-1)+1);
      Fs(3*(j-1)+2)=K_factor(j-1)*y(3*(j-2)+2)-K_factor(j)*y(3*(j-1)+2);
      Fs(3*(j-1)+3)=K_factor(j-1)*y(3*(j-2)+3)-K_factor(j)*y(3*(j-1)+3);
      Fd(3*(j-1)+1)=D_factor(j-1)*y(3*(j-2)+1)-D_factor(j)*y(3*(j-1)+1);
      Fd(3*(j-1)+2)=D_factor(j-1)*y(3*(j-2)+2)-D_factor(j)*y(3*(j-1)+2);
      Fd(3*(j-1)+3)=D_factor(j-1)*y(3*(j-2)+3)-D_factor(j)*y(3*(j-1)+3);
   end
end

%%%%%%%%%%%%%%%%%%%%%%%%%%%%%%%%%%%%%%%%%%%%%%%%%%%%%%%%%%%%%%%%%%%%%%%
% Electromagnetic Forces on Tether Lumped Masses

for j=1:n
   if j==1
      Fe(3*(j-1)+1)=0.5*current*(Bz*y(3*(j-1)+2)-By*y(3*(j-1)+3));
      Fe(3*(j-1)+2)=0.5*current*(Bx*y(3*(j-1)+3)-Bz*y(3*(j-1)+1));
      Fe(3*(j-1)+3)=0.5*current*(By*y(3*(j-1)+1)-Bx*y(3*(j-1)+2));
   else
      Fe(3*(j-1)+1)=0.5*current*
         (Bz*(y(3*(j-1)+2)+y(3*(j-2)+2))-By*(y(3*(j-1)+3)+y(3*(j-2)+3)));
      Fe(3*(j-1)+2)=0.5*current*
         (Bx*(y(3*(j-1)+3)+y(3*(j-2)+3))-Bz*(y(3*(j-1)+1)+y(3*(j-2)+1)));
      Fe(3*(j-1)+3)=0.5*current*
         (By*(y(3*(j-1)+1)+y(3*(j-2)+1))-Bx*(y(3*(j-1)+2)+y(3*(j-2)+2)));
   end
end
```

```
%%%%%%%%%%%%%%%%%%%%%%%%%%%%%%%%%%%%%%%%%%%%%%%%%%%%%%%%%%%%%%%%%%%%%%%
% Kane's Dynamical Equations

for j=1:n
   udot(3*(j-1)+1)=1/m(j)*(Fg(3*(j-1)+1)+Fs(3*(j-1)+1)+
         Fd(3*(j-1)+1)+Fe(3*(j-1)+1))+omega*u(3*(j-1)+2);
   udot(3*(j-1)+2)=1/m(j)*(Fg(3*(j-1)+2)+Fs(3*(j-1)+2)+
         Fd(3*(j-1)+2)+Fe(3*(j-1)+2))-omega*u(3*(j-1)+1);
   udot(3*(j-1)+3)=1/m(j)*(Fg(3*(j-1)+3)+Fs(3*(j-1)+3)+
         Fd(3*(j-1)+3)+Fe(3*(j-1)+3));
end

for j=1:n
   ydot(3*n+3*(j-1)+1)=udot(3*(j-1)+1);
   ydot(3*n+3*(j-1)+2)=udot(3*(j-1)+2);
   ydot(3*n+3*(j-1)+3)=udot(3*(j-1)+3);
end

ydot(6*n+1)=omega;

temp1 = u(1)-rk*omega*cos(phik)*sin(thetak)-Rdot;
temp2 = u(2)-R*omega+rk*omega*cos(phik)*cos(thetak);
temp3 = u(3);

ydot(6*n+2)= -temp1*cos(thetak)*cos(phik)-
         temp2*sin(thetak)*cos(phik)-temp3*sin(phik);
ydot(6*n+3)= temp1*sin(thetak)/(rk*cos(phik))-
         temp2*cos(thetak)/(rk*cos(phik));
```

```
ydot(6*n+4)= temp1*cos(thetak)*sin(phik)/rk+

         temp2*sin(thetak)*sin(phik)/rk-temp3*cos(phik)/rk;

%%%%%%%%%%%%%%%%%%%%%%%%%%%%%%%%%%%%%%%%%%%%%%%%%%%%%%%%%%%%%%%%%%%%%%%%%%%%

waitbar(t/t_final);

ydot=ydot';
```

APPENDIX B

EQUATIONS OF MOTION FOR ORBIT-BOOSTING TETHER MODEL IMPLEMENTED IN AUTOLEV

```
%electro.al
pause 0
newtonian N                % Earth centered inertial frame
points E                   % center of the Earth
particles P{5}
%
autoz on                   % automatic substitution on
constants RC, mu,K,C,L{4}  % R_cm, GMe, stiffness, damping, segment length
variables u{15}',q{15}'    % generalized speeds and generalized coordinates
specified stretch{4}'      % tether stretch and its rate
mass P1=M1,P2=M2,P3=M3,P4=M4,P5=M5         % masses for particles
%
% position vectors
p_E_P1>= q1*N1>+q2*N2>+q3*N3>
p_P1_P2>=q4*N1>+q5*N2>+q6*N3>
p_P2_P3>=q7*N1>+q8*N2>+q9*N3>
p_P3_P4>=q10*N1>+q11*N2>+q12*N3>
p_P4_P5>=q13*N1>+q14*N2>+q15*N3>
%
% kinematical differential equations
q1'=U1
q2'=U2
```

```
q3'=U3
q4'=U4
q5'=U5
q6'=U6
q7'=U7
q8'=U8
q9'=U9
q10'=U10
q11'=U11
q12'=U12
q13'=U13
q14'=U14
q15'=U15
%
% velocities
V_P1_N>=U1*N1>+U2*N2>+U3*N3>
uvp1>=unitvec(V_P1_N>)
V_P2_N>=V_P1_N>+U4*N1>+U5*N2>+U6*N3>
V_P3_N>=V_P2_N>+U7*N1>+U8*N2>+U9*N3>
V_P4_N>=V_P3_N>+U10*N1>+U11*N2>+U12*N3>
V_P5_N>=V_P4_N>+U13*N1>+U14*N2>+U15*N3>
%
% gravity forces        %mu=G*Me
%
up1>=unitvec(p_E_P1>)
FORCE(P1,-mu*M1*up1>/dot(p_E_P1>,p_E_P1>))             % gravity on P1
%
up2>=unitvec(p_E_P2>)
FORCE(P2,-mu*M2*up2>/dot(p_E_P2>,p_E_P2>))             % gravity on P2
```

```
%
FORCE(P3,-mu*M3*p_E_P3>/(dot(p_E_P3>,p_E_P3>))^1.5)      % gravity on P3
%
FORCE(P4,-mu*M4*p_E_P4>/(dot(p_E_P4>,p_E_P4>))^1.5)      % gravity on P4
%
FORCE(P5,-mu*M5*p_E_P5>/(dot(p_E_P5>,p_E_P5>))^1.5)      % gravity on P5
%
% aerodynamic drag
constants rho,cd,area
rhocda=rho*cd*area
FORCE(P4,-0.5*rhocda*mag(V_P4_N>)*V_P4_N>)  % drag in tetherlower half
FORCE(P5,-0.5*rhocda*mag(V_P5_N>)*V_P5_N>)

% spring forces
L12=MAG(p_P1_P2>)
stretch1=L12-L1
uvec1>=p_P1_P2>/L12
stretch1'=DOT((V_P2_N>-V_P1_N>),uvec1>)
FORCE(P1/P2,(-K*stretch1-C*stretch1')*uvec1>)  % spring force between P1,P2
%
L23=MAG(p_P2_P3>)
stretch2=L23-L2
uvec2>=p_P2_P3>/L23
stretch2'=DOT((V_P3_N>-V_P2_N>),uvec2>)
FORCE(P2/P3,(-K*stretch2-C*stretch2')*uvec2>)  % spring force between P2,P3
%
L34=MAG(p_P3_P4>)
stretch3=L34-L3
uvec3>=p_P3_P4>/L34
```

```
stretch3'=DOT((V_P4_N>-V_P3_N>),uvec3>)
FORCE(P3/P4,(-K*stretch3-C*stretch3')*uvec3>)  % spring force between P3,P4
%
L45=MAG(p_P4_P5>)
stretch4=L45-L4
uvec4>=p_P4_P5>/L45
stretch4'=DOT((V_P5_N>-V_P4_N>),uvec4>)
FORCE(P4/P5,(-K*stretch4-C*stretch4')*uvec4>)  % spring force between P4,P5
%
% electrodynamic forces
constants B0,Re,mue,gamma,delta % mue is electromagnetic constant for earth
%
frames I,J
simprot(N,I,3,gamma*t)       % I fixed in earth spinning with rate gamma
simprot(I,J,2,delta)         % J3 along earth's magnetic axis of tilt delta
%
constants Iamp
specified current  % electrodynamic force considered for tether upper half
current=Iamp
%
rm1>=p_E_P1>+0.5*L12*uvec1>
urm1>=unitvec(rm1>)
lam1=asin(dot(j3>,urm1>))
dp1>=cross(urm1>,unitvec(cross(urm1>,j3>)))

B1>=B0*(Re/mag(rm1>))^3*(cos(lam1)*dp1>+2*sin(lam1)*urm1>)
fm1>=current*L12*cross(uvec1>,B1>)
FORCE(P1,0.5*fm1>)                % electrodynamic force on P1
%
```

```
rm2>=p_E_P2>+0.5*L23*uvec2>
urm2>=unitvec(rm2>)
lam2=asin(dot(j3>,urm2>))
dp2>=cross(urm2>,unitvec(cross(urm2>,j3>)))

B2>=B0*(Re/mag(rm2>))^3*(cos(lam2)*dp2>+2*sin(lam2)*urm2>)
fm2>=current*L23*cross(uvec2>,B2>)
FORCE(P2,0.5*(fm1>+fm2>))         % electrodynamic force on P2
%
FORCE(P3,0.5*fm2>)                % electrodynamic force on P3
%
norm1>=cross(-uvec1>,uvp1>)/mag(cross(-uvec1>,uvp1>))
tau1>=cross(norm1>,-uvec1>)
%
uvp2>=unitvec(V_P2_N>)
norm2>=cross(-uvec2>,uvp2>)/mag(cross(-uvec2>,uvp2>))
tau2>=cross(norm2>,-uvec2>)
%
ZERO=FR()+FRSTAR()
%
KANE()     % Kane's Equations of Motion
%
% tether_IC.al has initial conditions computed exactly
%
% outputs
n>=cross(up1>,uvp1>)/mag(cross(up1>,uvp1>))
tau>=cross(n>,up1>)

yn=dot(p_P1_P5>,n>)
```

```
pvec>=p_P1_P5>-yn*n>
phi=atan(yn/mag(pvec>))*180/pi
x=dot(pvec>,tau>)
y=dot(pvec>,-up1>)
theta=atan(x/y)*180/pi
ndef>=cross(unitvec(p_P1_p3>),unitvec(p_P1_p5>))
tdef>=cross(unitvec(p_P1_p5>),ndef>)
mpdefl=dot(p_P1_P3>,tdef>)

points cm
v_e_n>=0>
p_e_cm>=cm(e)
orbalt=(mag(p_e_cm>)-6.378140e6)/1000
ftau=dot(fm1>,tau1>)+dot(fm2>,tau2>)

xo=dot(p_e_cm>,n1>)
yo=dot(p_e_cm>,n2>)
zo=dot(p_e_cm>,n3>)
%
input B0=3.5e-5,Re=6.378140e6
input Iamp=1.5
input mu=3.986005e14
input Rc=6.378140e6+500e3
input mue=7.943e15,gamma=2*pi/(24*3600),delta=(11/180)*pi
input K=8 %1 mm dia,E=6894e7 Pascals,L=5000m
input C=0.0465
input L1=5000,L2=5000,L3=5000,L4=5000
input M1=302.5,M2=5,M3=5,M4=5,M5=7.5
input cd=2.2,area=35,rho=1.e-12
```

```
%
% input values were separately computed by tether_ic.al
input q1=-3126668.177573941
input q2=3126668.177573942
input q3=5269668.07929776
input q4=2272.711018229637
input q5=-2272.711018229637
input q6=-3830.413726705
input q7=2272.711018229637
input q8=-2272.711018229637
input q9=-3830.41372670567
input q10=2272.711018229637
input q11=-2272.711018229637
input q12=-3830.41372670567
input q13=2272.711018229637
input q14=-2272.711018229637
input q15=-3830.41372670567
%
input u1=-5383.648529562682
input u2=-5383.648529562681
input u3=0
input u4=3.913263780010931
input u5=3.91326378001093
input u6=0
input u7=3.913263780010931
input u8=3.91326378001093
input u9=0
input u10=3.913263780010931
input u11=3.91326378001093
```

```
input u12=0

input u13=3.913263780010931

input u14=3.91326378001093

input u15=0

%

input tfinal=18000,integstp=5

%

output t,orbalt,ftau,current

output t,theta,phi,mpdefl

output t,xo,yo,zo

%

code dynamics(),electro.c,subs
```

REFERENCES

[1] Alli, H. and Singh, T., "On the feedback control of the wave equation," *Sound and Vibration*, vol. 234, no. 4, pp. 625–640, 2000.

[2] Banerjee, A., Singhose, W., and Blackburn, D., "Orbit boosting of an electrodynamic tethered satellite with input-shaped current," in *2005 AAS/AIAA Astrodynamics Specialists Conference*, (Lake Tahoe, CA), 2005.

[3] Banerjee, A. K., Pedreiro, N., and Singhose, W. E., "Vibration reduction for flexible spacecraft following momentum dumping with/without slewing," *AIAA Journal of Guidance, Control, and Dynamics*, vol. 24, no. 3, pp. 417–427, 2001.

[4] Blackburn, D., Singhose, W., Kitchen, J., Patrangenaru, V., Lawrence, J., Kamoi, T., and Taura, A., "Advanced input shaping algorithm for nonlinear tower crane dynamics," in *8th International Conference on Motion and Vibration Control*, (KAIST, Daejeon, Korea), 2006.

[5] Bosscher, P. and Ebert-Uphoff, I., "Wrench-based analysis of cable-driven robots," in *IEEE International Conference on Robotics and Automation*, (New Orleans, LA), pp. 4950–4955, 2004.

[6] Bostelman, R., Albus, J., Dagalakis, N., Jacoff, A., and Gross, J., "Applications of the nist robocrane," in *5th International Symposium on Robotics and Manufacturing*, (Maui, HI), 1994.

[7] Estes, R. D., Lorenzini, E. C., Sanmartín, J., Peláez, J., Martínez-Sánchez, M., Johnson, C. L., and Vas, I. E., "Bare tethers for electrodynamic spacecraft propulsion," *Journal of Spacecraft and Rockets*, vol. 37, no. 2, pp. 205–211, 2000.

[8] Estes, R. D., Sanmartín, J., and Martínez-Sánchez, M., "Performance of bare-tether systems under varying magnetic and plasma conditions," *Journal of Spacecraft and Rockets*, vol. 37, no. 2, pp. 197–204, 2000.

[9] Hong, K.-T. and Hong, K.-S., "Input shaping and vsc of container cranes," in *IEEE International Conference on Control Applications*, (Taipei, Taiwan), pp. 1570–1575, 2004.

[10] Hu, Q. and Ma, G., "Vibration suppression of flexible spacecraft during attitude maneuvers," *AIAA Journal of Guidance, Control, and Dynamics*, vol. 28, no. 2, pp. 377–380, 2005.

[11] Huey, J. and Singhose, W., "The application of input shaping to wire-driven mechanisms," in *6th International Conference on Motion and Vibration Control*, (Saitama, Japan), 2002.

[12] Hyde, J. M. and Seering, W. P., "Using input command pre-shaping to suppress multiple mode vibration," in *IEEE Int. Conf. on Robotics and Automation*, vol. 3, (Sacramento, CA), pp. 2604–2609, IEEE, 1991.

[13] Kawamura, S., Choe, W., Tanaka, S., and Pandian, S. R., "Development of an ultrahigh speed robot falcon using wire drive system," in *IEEE International Conference on Robotics and Automation*, vol. 1, pp. 215–220, 1995.

[14] Kojima, H., Iwasaki, M., Fujii, H. A., Blanksby, C., and Trivailo, P., "Nonlinear control of librational motion of tethered satellites in elliptic orbits," *Journal of Guidance, Control, and Dynamics*, vol. 27, no. 2, pp. 229–239, 2004.

[15] Lawrence, J., Fatkin, B., Singhose, W., Weiss, R., Erb, A., and Glauser, U., "An internet-driven tower crane for dynamics and controls education," in *7th IFAC Symposium on Advances in Control Education*, (Madrid, Spain), 2006.

[16] Lawrence, J. and Singhose, W., "Design of a minicrane for education and research," in *6th International Workshop on Research and Education in Mechatronics*, (Annecy, France), pp. 254–259, 2005.

[17] Mankala, K. K. and Agrawal, S. K., "Equilibrium-to-equilibrium maneuvers of rigid electrodynamic tethers," *AIAA Journal of Guidance, Control, and Dynamics*, vol. 28, no. 3, pp. 541–545, 2005.

[18] Peláez, J. and Andres, Y. N., "Dynamic stability of electrodynamic tethers in inclined elliptical orbits," *AIAA Journal of Guidance, Control, and Dynamics*, vol. 28, no. 4, pp. 611–622, 2005.

[19] Robertson, M. and Singhose, W., "Evaluation of analytic deflection-limiting commands," in *IFAC World Congress*, (Prague, Czech Republic), 2005.

[20] Robertson, M. J. and Singhose, W. E., "Closed-form deflection-limiting commands," in *American Control Conference*, (Portland, OR, USA), pp. 2104–2109, 2005.

[21] Robertson, M. J. and Singhose, W. E., "Robust analytic deflection-limiting commands," in *American Control Conference*, 2006.

[22] Singer, N., Singhose, W., and Kriikku, E., "An input shaping controller enabling cranes to move without sway," in *ANS 7th Topical Meeting on Robotics and Remote Systems*, vol. 1, (Augusta, GA), pp. 225–231, 1997.

[23] Singer, N. C. and Seering, W. P., "Preshaping command inputs to reduce system vibration," *ASME Journal of Dynamic Systems, Measurement, and Control*, vol. 112, pp. 76–82, 1990.

[24] Singer, N. C. and Seering, W. P., "An extension of command shaping methods for controlling residual vibration using frequency sampling," in *IEEE International Conference on Robotics and Automation*, vol. 1, (Nice, France), pp. 800–805, IEEE, 1992.

[25] Singhose, W., Banerjee, A. K., and Seering, W. E., "Slewing flexible spacecraft with deflection limiting input shaping," *AIAA Journal of Guidance, Control, and Dynamics*, vol. 20, no. 2, pp. 291–298, 1997.

[26] Singhose, W., Crain, E., and Seering, W., "Convolved and simultaneous two-mode input shapers," *IEE Proceedings - Control Theory Applications*, vol. 144, no. 6, pp. 515–520, 1997.

[27] Singhose, W., Seering, W., and Singer, N., "Residual vibration reduction using vector diagrams to generate shaped inputs," *Journal of Mechanical Design, Transactions of the ASME*, vol. 116, no. 2, pp. 654–659, 1994.

[28] Singhose, W., Singer, N., and Seering, W., "Time-optimal negative input shapers," *ASME Journal of Dynamic Systems, Measurement, and Control*, vol. 119, pp. 198–205, 1997.

[29] Singhose, W., Biediger, E. O., and Chen, Y.-H., "Reference command shaping using specified-negative-amplitude input shapers for vibration reduction," *ASME Journal of Dynamic Systems, Measurement, and Control*, vol. 126, pp. 210–214, 2004.

[30] Singhose, W., Bohlke, K., and Seering, W., "Fuel-efficient pulse command profiles for flexible spacecraft," *AIAA Journal of Guidance, Control, and Dynamics*, vol. 19, no. 4, pp. 954–960, 1996.

[31] Singhose, W., Derezinski, S., and Singer, N., "Extra-insensitive input shapers for controlling flexible spacecraft," *AIAA Journal of Guidance, Control, and Dynamics*, vol. 19, no. 2, pp. 385–391, 1996.

[32] Singhose, W. E., Seering, W. P., and Singer, N. C., "Input shaping for vibration reduction with specified insensitivity to modeling errors," in *Japan-USA Symposium on Flexible Automation*, 1996.

[33] Smith, O. J. M. in *Feedback Control Systems*, pp. 331–345, New York: McGraw-Hill Book Company, Inc., 1958.

[34] Smith, R., Starr, G. P., Lumia, R., and Wood, J., "Preshaped trajectories for residual vibration suppression in payloads suspended from multiple robot manipulators," in *IEEE International Conference on Robotics and Automation*, (New Orleans, LA), pp. 1599–1603, 2004.

[35] Somenzi, L., Iess, L., and Peláez, J., "Linear stability analysis of electrodynamic tethers," *AIAA Journal of Guidance, Control, and Dynamics*, vol. 28, no. 5, pp. 843–849, 2005.

[36] Sorensen, K., "Conceptual design and analysis of an mxer tether boost station," in *AIAA/SME/SAE/ASEE Joint Propulsion Conference*, (Salt Lake City, UT), 2001.

[37] Starr, G. P., "Swing-free transport of suspended objects with a path-controlled robot manipulator," *Journal of Dynamic Systems, Measurement, and Control*, vol. 107, pp. 97–100, 1985.

[38] Tallman, G. H. and Smith, O. J. M., "Analog study of dead-beat posicast control," *IRE Transactions on Automatic Control*, pp. 14–21, 1958.

[39] Tragesser, S. G. and San, H., "Orbital maneuvering with electrodynamic tethers," *AIAA Journal of Guidance, Control, and Dynamics*, vol. 26, no. 5, pp. 805–810, 2003.

[40] Vas, I. E., Kelly, T. J., and Scarl, E. A., "Space station reboost with electrodynamic tethers," *Journal of Spacecraft and Rockets*, vol. 37, no. 2, pp. 154–164, 2000.

[41] Watanabe, T., Makida, T., Fujii, H. A., Kojima, H., and Singhose, W., "An application of input shaping for electroynamic tether system," in *AIAA/AAS Astrodynamics Specialists Conference*, (Providence, Rhode Island), 2004.

[42] Williams, P., "Optimal orbital transfer with electrodynamic tether," *AIAA Journal of Guidance, Control, and Dynamics*, vol. 28, no. 2, pp. 369–372, 2005.

[43] Williams, P., Blanksby, C., and Trivailo, P., "The use of electromagnetic lorentz forces as a tether control actuator," in *53rd International Astronautical Congress: The World Space Congress*, (Houston, Texas), 2002.

[44] Williams, P., Watanabe, T., Blanksby, C., Trivailo, P., and Fujii, H. A., "Libration control of flexible tethers using electromagnetic forces and movable attachment," *AIAA Journal of Guidance, Control, and Dynamics*, vol. 27, no. 5, pp. 882–897, 2004.

[45] Yang, K.-J., Hong, K.-S., and Matsuno, F., "Robust boundary control of an axially moving string by using a pr transfer function," *IEEE Transactions on Automatic Control*, vol. 50, no. 12, pp. 2053–2058, 2005.

[46] Zhang, W. and Chen, L.-Q., "Vibration control of an axially moving string system: Wave cancellation method," *Applied Mathematics and Computation*, vol. 175, pp. 851–863, 2006.